A genotoxic antibody drug conjugate targeting CD276/B7H3 demonstrates efficacy across multiple biomarker defined classes of treatment refractory metastatic prostate cancer

Authors: Supreet Agarwal[1], Lei Fang[1], Kerry McGowen[1], JuanJuan Yin[1], Joel Bowman[1], Anson T. Ku[1], Aian Neil Alilin[1], Eva Corey[2], Martine Roudier[2], Lawrence True[3], Ruthy Dumpit[4], Ilsa Coleman[4], John Lee[4], Peter S. Nelson[4], Brian J. Capaldo[1], Ilya S. Senatorov[1], Adam G. Sowalsky[1], Elaine M Hurt[5], Kathleen Kelly[1*]

Affiliations:

[1]Laboratory of Genitourinary Cancer Pathogenesis, Center for Cancer Research, National Cancer Institute, NIH; Bethesda, Maryland, USA.

[2]Department of Urology, University of Washington, Seattle, WA 98195

[3]Department of Laboratory Medicine and Pathology, University of Washington, Seattle, WA 98195

[4]Divisions of Human Biology and Clinical Research, Fred Hutchinson Cancer Research Center, Seattle, WA 98119

[5]AstraZeneca; Gaithersburg, Maryland, USA.

*Corresponding author. Email: kellyka@mail.nih.gov

One Sentence Summary: B7H3-PBD-ADC sensitivity in metastatic prostate cancer is associated with replication stress, SLFN11 expression related to interferon signaling, and alterations in specific DNA repair factors.

ABSTRACT

B7H3, a cell surface protein often associated with higher grade solid tumors of various origins, is an attractive therapeutic target due to its frequent upregulated expression relative to normal tissue. In a large cohort of treatment-resistant, metastatic castrate resistant prostate cancer (mPC) patient derived xenografts and organoids, we present a comprehensive therapeutic and biomarker analysis. The 26 models tested encompass the heterogeneous genomic and histological categories of clinical mPC. *In vitro* and *in vivo* treatment with an anti-B7H3 targeted antibody conjugated to a pyrrolobenzodiazepine (PBD) cytotoxic agent were efficacious in 70% of models. All models expressed some B7H3 protein, the levels of which did not correlate with responses. Underlying susceptibilities to B7H3-PBD-ADC exposure were observed as multiple imperfectly overlapping classes of biomarkers, unrelated to androgen receptor dependence and substantially expanded beyond current homologous repair deficiencies. *RB1* deficiency and/or replication stress, particularly prominent in small cell neuroendocrine prostate cancer (SCNPC), predicted responsiveness. The presence of SLFN11 in SCNPC and adenocarcinoma models correlated perfectly with vulnerability, although an absence of SLFN11 was not predictive. Of particular interest, an elevated interferon signature in adenocarcinomas, associated with alteration of wild type *TP53*, was quantitatively correlated with responsiveness. Finally, we also observed that susceptible models uniquely associated with the loss of select downstream DNA repair proteins. The above biomarkers are expressed *in toto* in about 70% of mPC clinical samples, suggesting broad potential for mechanistically complementary treatment of tumors escaping current regimens.

INTRODUCTION

Metastatic prostate cancer (mPC) remains a lethal disease accounting for more than 30,000 deaths annually in the United States *(1)*. The use of androgen deprivation therapy (ADT) and androgen receptor (AR) signaling inhibitors (ARSI) have significantly prolonged the survival of patients with mPC in both pre- and post- chemotherapy settings. Unfortunately, durable complete responses are uncommon and with the development of castration resistant prostate cancer (mCRPC) mortality rates approach 100%. Continuously evolving acquired resistance mechanisms include frequent AR mutations and structural genomic alterations that drive an AR-active adenocarcinoma phenotype (ARPC). Less common, but increasing in frequency, are resistance mechanisms that bypass an AR requirement though lineage plasticity with the emergence of phenotypes spanning neuroendocrine phenotypes (NEPC) and various rarer histologies *(2)*. Since the vast majority of mPC phenotypes eventually resist all currently approved therapeutics, new treatment strategies are essential.

A promising approach for developing effective and less toxic therapies for mPC involves selectively targeting tumor cells via tumor-specific cell surface proteins and cognate antigens. Exploiting prostate specific membrane antigen (PSMA) to deliver high dose radiation to tumor cells overexpressing PSMA, PSMA-Lu177, has recently gained FDA approval for the treatment of mPC *(3)*. Strategies utilizing PSMA and other cell surface targets such as PSCA, TROP2, STEAP1, and CEACAM5 include the development of bispecific T-cell engaging antibodies (BITEs), chimeric antigen receptor T cells (CART) and antibody drug conjugates (ADCs) *(4–6)*. ADCs combine the high target specificity of a monoclonal antibody with a cytotoxic agent for targeted killing of tumor cells. ADCs are rapidly internalized, releasing the antibody-linked payload to induce cell death. Several classes of cytotoxic chemicals have been utilized in ADC designs, though most are either potent microtubule poisons or inducers of DNA damage *(7)*.

Pyrrolobenzodiazepines (PBD) are DNA minor-groove crosslinking agents that have been used as genotoxic payloads for several clinical grade ADCs *(8)*. PBD dimers bind in a sequence specific manner to form inter-strand crosslinks (ICLs) leading to double strand DNA breaks due to replication fork arrest *(8)*. Previous studies have shown that tumors with enhanced replication stress are more sensitive to deleterious replication fork blocks caused by topoisomerase inhibitors, PARP inhibitors, and platinum DNA cross-linking agents *(9, 10)*. Characterizing the utility of PBD dimers for the treatment of cancers exhibiting replication stress is a question of interest. The long term success of ADCs with PBD or other payloads will be greatly enhanced by an informed strategy to stratify patients based on robust biomarkers of response and resistance.

In addition to differential cell vulnerabilities relating to the type of ADC payload, the selective expression of antigens targeted by an ADC is an important determinant of efficacy and the ascertainment of a favorable therapeutic window. In the setting of mPC, PSMA is expressed by the majority, though not all AR active PCs, but emerging treatment-resistant phenotypes such as small cell neuroendocrine PC (SCNPC) generally do not express PSMA, prompting a search for alternate targets. CD276/B7H3 is a type I transmembrane protein normally involved in regulating immune cell function with additional roles promoting migration, invasion, and chemoresistance of tumor cells. B7H3 is overexpressed in several solid tumors and often correlated with poor survival and higher tumor grade *(11–13)*. The preferential overexpression of B7H3 on cancer cells and tumor vasculature supports efforts to develop antibody-based therapeutics that exploit both the cell type-specific targeting and the functional properties of B7H3 *(14)*.

In this study, we evaluated a therapeutic strategy targeting B7H3 for the treatment of mPC.

We profiled a spectrum of metastatic mPC tumors to assess the heterogeneity of B7H3 expression with respect to metastatic site and tumor phenotype. We tested a humanized B7H3-ADC armed with PBD payload across a range of molecularly characterized, clinically relevant mPC PDX and organoid models that reflect the diversity of human mPCs. Although we anticipated that DNA repair deficiencies and levels of B7H3 expression would associate with responses, we unexpectedly uncovered additional independent and linked biomarkers that represent vulnerabilities derived from more than one sensitivity or resistance pathway. These analyses demonstrate how a diverse cohort of mPCs distribute into distinct biomarker classes that reflect ADC mechanisms of action. Collectively the results have the potential to inform patient selection for prospective trials and contribute to the interpretation of patient response and resistance outcomes.

RESULTS

B7H3 is expressed across a range of mPC phenotypes and diverse metastatic sites.

To assess the potential clinical utility of targeting B7H3 as a treatment strategy for advanced prostate cancer, we evaluated the expression of B7H3 in treatment refractory prostate cancer metastasis. We first quantitated B7H3 transcript abundance in 185 tumors from 98 patients with mPC using RNAseq measurements. We also categorized each tumor into phenotypic categories based on gene expression signatures reflecting AR signaling and neuroendocrine (NE) pathway activity. Overall, the vast majority of tumors expressed B7H3 transcripts and there was limited variation within or between mPC phenotypes (**Fig. 1, A-C**). The mean fragments per kilobase per million reads (Log_2 FPKM) for AR+/NE- tumors was 4.27 compared to 3.78 for AR-/NE+ tumors (P=0.046). In contrast, PSMA expression varied substantially both within a phenotype

and between phenotypes: mean Log_2FPKM of 5.46 in AR+/NE- versus 0.01 for AR-/NE+ (P=1x10^{-9}). We also evaluated the intra-individual heterogeneity of B7H3 by measuring B7H3 transcript levels in multiple tumors acquired from the same patient. With few exceptions, there was a tight distribution of B7H3 expression within individuals (**Fig. S1A**).

We next evaluated B7H3 protein expression across a cohort of PC metastases using a tissue microarray comprised of tumors from 58 patients (range of 2 to 4 tumors per patient). Overall, B7H3 protein exhibited more variation compared to transcript expression: of 181 tumors evaluated, 152 expressed B7H3 (H-score > 20) and 29 lacked expression (**Fig. 1, D and E**). B7H3 was detected across diverse metastatic sites with bone metastases exhibiting the highest levels (**Fig. 1E**). Tumors categorized as AR+/NE- ARPC generally expressed higher B7H3 levels compared to other phenotypes, but a subset of AR-/NE+ SCNPC and AR-/NE- tumors also expressed B7H3 (**Fig. 1, F and G**). Collectively, these results indicate that B7H3 may represent a target for antigen-directed therapeutics across a range of mPC phenotypes.

B7H3 is expressed across mPC models representing diverse genotypes and phenotypes

To determine if preclinical models of mPC are appropriate for assessments of B7H3 directed ADC treatment, we analyzed B7H3 expression across a panel of models representing the genomic and phenotypic heterogeneity of patient tumors. The 26 models tested in this study comprise tumors of adenocarcinoma phenotype with AR signaling (intact; n= 13, experimentally castrate resistant(CR); n=6) (denoted as ARPC) as well as $AR^{NEG/VERY\ LOW}$ non-neuroendocrine prostate cancer (n=2)(denoted as DNPC) *(2)* and small cell neuroendocrine prostate cancer (denoted as SCNPC; n=5) (the latter two groups collectively categorized as non-ARPC) (**Fig. 2A)**. The models included were primarily from the LuCaP PDX series *(15)* and also included 2

NCI mPC patient biopsy-derived organoids (PDOs) of the ARPC phenotype *(16)*. B7H3 transcript levels were quantified in PDX tumors, in PDX-derived organoids (PDXOs), and in PDOs. Although most models clustered within a 2-fold range of expression within tumor lines, there was altogether approximately a 10-fold variation in levels across tumor lines. There was no significant difference in median RNA expression between the ARPC and non-ARPC phenotypes (**Fig. 2, A and B**). PDXOs maintained similar *B7H3* RNA as their corresponding PDX tumor tissue (**Fig. S1B**).

We used a quantitative immunoblot technique to determine the relative amount of total B7H3 protein expressed in each model. Although B7H3 protein was evident in all models, there was a >30- fold variation in expression (**Fig. 2C** and **Fig. S1C**). ARPC models demonstrated a range of expression clustering as a high group ($B7H3^{Hi}$) and an intermediate to low group, the latter of which overlapped in median level with the non-ARPC group (**Fig. 2C**). B7H3 mRNA levels were not strongly correlated with B7H3 protein levels in models of either phenotype (**Fig. S1D**) consistent with post-transcriptional regulation *(13)*. FACS analysis of B7H3 cell surface expression in organoid derived cells, gated for human-specific EpCam expression, showed that 80-100% of the cells expressed B7H3 protein, although the median fluorescence intensity was variable across the models tested (n=9) (**Fig. 2, D** and **E**, and **Fig. S2A**). B7H3 cell surface expression was well correlated with total B7H3 protein (**Fig. 2F**). As AR signaling is a major determinant of ARPC phenotypic subclasses, we determined the relationship of B7H3 RNA and protein to AR target gene output. However, consistent with the analyses of human mPC tumors (**Fig. 1**), there was no correlation of B7H3 protein levels with AR signature scores (**Fig. S2B**).

B7H3-PBD-ADC is cytotoxic for defined subclasses of prostate cancer

We next sought to determine the efficacy of an ADC directing the genotoxic PBD (B7H3-PBD-ADC) to mPC cells. We compared the targeted delivery of PBD via B7H3-PBD-ADC relative to the non-targeted control R347-PBD-ADC across a panel of mPC organoids where phenotype, genotype, and B7H3 levels were established (**Fig. 3, A and B, Fig. S3A, and data file S1**). All non-ARPC models were highly sensitive to the B7H3-PBD-ADC with normalized AUC (nAUC) ranging from 0.2-0.5 and IC50 from 0.03-2.08 ng/ml (**Fig. 3C and Table 1**). In contrast, the ARPC models displayed a broad range of responses, with nAUC ranging from 0.3 to 1 and displaying less steep dose response slopes in responders compared to the non-ARPC models (**Fig. 3B and Fig. 3C**). The relative dose required for cytotoxicity in comparing targeted B7H3-PBD-ADCs and control R347-PBD-ADCs was a minimum of 1000-fold for the most sensitive models, while the majority of models were unaffected by even the highest concentration of R347-PBD (4 mg/ml) (**Fig. 3B and Fig. S3, B and C**).

Interestingly, there were two categories of ARPC responders to B7H3-PBD-ADCs, which segregated with B7H3 protein expression levels. Organoids with the highest B7H3 protein expression (LuCaPs-35CR, 170.2 and 141, and NCI-PC155) were the most sensitive among the ARPC models (**Fig. 3, C and D**). There were no non-responders among the highest B7H3 expressing ARPC models. However, responses in the majority of the models were not correlated with B7H3 expression and thus appeared to be governed by other tumor biological properties. The ARPC cluster with low to medium B7H3 expression contained responder (labeled as “R”) and non-responder (labeled as “NR”) models. Notably, the median B7H3 protein expression in the responders was not significantly different from non-responder ARPC models or from responder non-ARPC models (**Fig. 3C**).

To establish specificity, we assessed whether B7H3 protein expression is necessary for ADC activity. CRISPR/Cas9 was used to generate B7H3 null organoid cells in LuCaP 145.2 and NCI-PC155 models. Because mPC organoids cannot be cloned, following B7H3 guide transduction into Cas9 expressing organoids, cells were sorted after several generations of growth based upon B7H3 expression (**Fig. 3, E and F**). The loss of B7H3 in B7H3^{NEG} LuCaP 145.2 did not result in any discernable difference in growth compared to B7H3^{+} organoids (**Fig. S3D**), indicating that B7H3 expression does not affect autonomous growth rate. Consistent with this, dropout screens utilizing 2 separate B7H3-directed guides in LuCaP 145.2 and LuCaP 173.1 organoids demonstrated no growth selectivity across the entire population (**Fig. S3E**). Importantly, loss of B7H3 in 145.2 organoids abrogated response to B7H3-PBD-ADC at concentrations less than 0.25 ug/ml *in vitro*, demonstrating a >400 fold increased IC50 compared to B7H3-WT organoids (**Fig. 3G**). However, we observed cytotoxic effects of the B7H3-PBD-ADC at higher concentrations of 1ug/ml and 4ug/ml, probably resulting from B7H3^{+} contaminants in the B7H3^{-} sorted population as well as likely bystander effects from free PBD *(14)*. B7H3-PBD-ADC specificity *in vivo* was confirmed using organoid derived xenograft models (ODXs) from sorted B7H3^{+} and B7H3^{-} LuCaP 145.2 organoids. B7H3^{-} ODXs displayed no response to the B7H3-PBD-ADC (bottom panel), whereas significant tumor regression was observed in B7H3^{+} tumors (top panel) compared to vehicle treated or negative control R347-PBD-ADC treated mice (**Fig. 3H**). Finally, loss of B7H3 protein in NCI-PC155 patient derived adenocarcinoma organoids substantially reversed B7H3-PBD-ADC sensitivity (**Fig. 3, I and J**). These results demonstrate that the B7H3-PBD-ADC has specific activity against B7H3 expressing mPC organoids over a broad range of tested concentrations.

B7H3-PBD-ADC response is associated with *RB1* deficiency and replication stress

An inspection of the model genotypes relative to B7H3-PBD-ADC efficacy to identify predictive response characteristics revealed that combined alterations of *RB1* and *TP53* were strongly correlated with responsiveness to B7H3-PBD-ADC treatment. Indeed, *RB1* homozygous deletion and *TP53* alterations, either deletion or mutation, occur in all the non-ARPC models (**Fig. 4, A and B, and Table 1**). Of interest, there also was an enrichment for *TP53*^{WT} alleles in 6/8 ARPC non-responder models compared to only 1/11 responder ARPC models. Further, *RB1* function was analyzed across the models using RB signature score that captures transcriptional networks related to RB1 functional inactivation. The RB signature score was linearly related to B7H3-PBD-ADC sensitivity as measured by AUC in organoid models, suggesting not only a categorical relationship but also a quantitatively determined sensitivity (**Fig. 4C**).

We experimentally validated *RB1* levels as a determinant for B7H3-PBD-ADC responses by depletion via doxycycline-induced shRNA in the non-responsive, *TP53*^{WT} LuCaP 167 ARPC organoid model (**Fig. 4D and Fig. S4A**). Consistent with the results across the various models, *RB1* depletion resulted in increased B7H3-PBD-ADC cytotoxicity in LuCaP 167 organoids, demonstrating *RB1* levels as an independent factor in determining B7H3-PBD-ADC sensitivity (**Fig. 4E**).

RB1 loss is associated with replication stress, and not unexpectedly, replication-stress induced pathways also correlated with the strength of B7H3-PBD-ADC responses. We used a replication stress signature score (RepStress score), modified for prostate cancer based on DNA damage and cell cycle pathways involved in replication stress, and analyzed association with B7H3-PBD sensitivity (**Fig. 5A**). Across all models, including ARPC and non-ARPC groups, a

high RepStress score was significantly correlated with higher sensitivity to B7H3-PBD-ADC (**Fig. S4B**), a finding which is strongly determined by loss of RB functionality (**Fig. S4C**). For the ARPC models only, the majority of the ARPC responders ("ARPC-R") had similar replication stress scores to non-responders ("ARPC-NR") with the exception of two responder $RB1^{WT}$ models (LuCaPs 23.1 and 170.2) demonstrating high outlier RepStress scores (**Fig. 5B**). This implies that PBD sensitivity of mPC adenocarcinoma models with functional RB1 is often governed by factors in addition to replication stress. Consistent with the phenotyping of various ARPC and non-ARPC models relative to RepStress, there was almost complete overlap in responsiveness to B7H3-PBD-ADC and other RepStress sensitive drugs including Topotecan, Cisplatin, and Mitomycin C (**Fig. S4D**). However, organoid models were more sensitive to B7H3-PBD compared to the other drugs that target RepStress.

Chronic interferon signaling and SLFN11 expression are predictors of B7H3-PBD-ADC response in mPCs with AR activity.

To address broadly predictive biomarkers in ARPC, the most common clinical phenotype of mCRPC, we analyzed differentially expressed signaling pathways in responder and nonresponder ARPC models. Correlation analysis with single sample gene set enrichment scores identified interferon response gene signatures as the topmost correlated signaling pathways for B7H3-PBD-ADC sensitivity (nAUC) for ARPC models (**Fig. 5C**). As shown in Figure 5D, an IFN response signature optimized for mPC (see supplementary methods) was highly correlated with B7H3-PBD-ADC responsiveness for ARPC models. Of interest, the ARPCs exhibiting the highest IFN response signatures (LuCaPs 23.1, 35CR, 141CR, and 170.2) expressed RB1 protein but lacked WT TP53 protein expression (**Fig. 4B**). Other than alterations in *TP53*, these models

do not have obvious mutational patterns in common nor is RepStress a common characteristic. Considering all AD models, loss of WT *TP53* was significantly associated with high IFN signature score (**Fig. 5D**, Wilcoxon test, $P = 0.008$).

To further delineate the role of specific interferon stimulated genes (ISGs) that may be contributing to B7H3-PBD-ADC response, we analyzed the gene expression profiles of ARPC models (n = 17). Differential expression analyses comparing ARPC responders (n = 9) and non-responders (n=8) revealed several ISGs among the top 20 differentially upregulated genes in responders including *UBE2L6*, *PSMB9*, and *SLFN11* while *CDKN1A* and *ABCB5* were notably downregulated (**Fig. 5E and data file S2**). Upregulation in ARPC responder models of SLFN11, a DNA/RNA helicase, was of particular interest as it is a known sensitizer for toxicity mediated by specific DNA damaging agents *(17, 18)*. Importantly, loss of SLFN11 has been specifically identified in experimentally induced PBD-resistant cell lines *(19)*. *SLFN11* is a non-classical interferon (IFN)-response gene, and indirect effects of IFN signaling likely contribute to contextual SLFN11 expression *(17)*. As expected, in the phenotypically heterogeneous models analyzed here, $SLFN11^{NEG}$ models demonstrated a significantly lower median IFN signature score than $SLFN11^{+}$ models (**Fig. 5F**). SLFN11 expression predicted response in 13 of 13 ARPC models, while lack of SLFN11 expression was not predictive (5 responders out of 13 $SLFN11^{NEG}$ models) (**Fig. 5G, R(-) group**). Although the majority (6/9) of RB1 deficient models were $SLFN11^{+}$ (**Fig. 4B**), RB1 deficient models were responsive to B7H3-PBD-ADC independent of SLFN11 expression.

ATR defects and _CHD1_ loss associate with synthetic lethal responses to DNA damage induced by B7H3-PBD-ADC treatment in SLFN11-negative ARPC.

While metrics of replication stress, high B7H3 expression and SLFN11/ISGs explained the responses of most tumors to B7H3-PBD-ADC treatment, there were several outliers where these features did not discriminate outcomes. For example, LuCaPs 141 and 141CR, and NCI-PC-155 categorized as responders, but are *RB1*^{WT} and SLFN11^{NEG} (**Fig. 4B and Fig. 5G**). Because ATR loss of function is a sensitizing factor for PBD responsiveness *(19)*, we considered pathway components upstream and downstream of the ATR pathway (**Fig. 4B**). Immunoblot analyses of mPC organoid models demonstrated variability in baseline ATM and ATR levels, although there were no correlations with PBD responsiveness. Increased baseline expression of the ATR target, pCHK1, was observed in *RB1* null models, most likely indicating RepStress; however, consistent with transcriptomic RepStress scoring in ARPC *RB1*^{WT} models, there were no correlations between pCHK1 and responses to B7H3-PBD-ADC treatment (**Fig. 4B**).

To analyze the functionality of the DNA damage-initiated ATR pathway, we evaluated CHK1/RPA phosphorylation in ARPC organoids of B7H3-PBD-ADC responders: LuCaP 77 (*RB1*^{WT}, SLFN11^{+}), LuCap 141CR and NCI-PC155 (*RB1*^{WT}, SLFN11^{NEG}) and the non-responder LuCaP 167 (*RB1*^{WT}, SLFN11^{NEG}). Functional ATR was evident in response to topotecan and B7H3-PBD-ADC in the various models, although reduced to near undetectable levels in both responder NCI-PC155 and non-responder LuCaP 167 (**Fig. S5, A-D**). Importantly, NCI-PC155 had significantly higher topotecan and B7H3-PBD-ADC induced DNA damage (γH2AX) compared to LuCaP 167 (**Fig. S5, A-B**). These data suggest that NCI-PC155 likely demonstrates increased PBD sensitivity because of very weak ATR signaling. By contrast, since non-responsive LuCaP 167 showed no evidence of PBD-mediated DNA damage, there may have been no ATR activation due to a lack of drug exposure, suggesting an active drug efflux mechanism. However, none of the previously identified transporters of PBD (*ABCG2, ABCB1,*

ABCC2, and SLC46A3) correlated with responsiveness in the extensive mPC cohort tested here (**Fig. S4E**). These data introduce the possibility that previously unappreciated drug efflux transporter(s) may also contribute to the PBD warhead sensitivity. It should be noted that pre-existing, baseline DNA damage was not associated with PBD responsiveness as determined by γH2AX levels across the various models (**Fig. 4B**).

As the SLFN11^{NEG} LuCaP 141CR model had an intact ATR pathway, we considered other DNA repair biomarkers. Importantly, we observed loss of *CHD1* RNA and protein in LuCaPs 141 and 141CR (**Fig. 4B**). CHD1 depleted cells are generally hypersensitive to DNA cross-linking agents because of defects in homologous recombination mediated repair *(20, 21)*, and in clinical mPC, *CHD1* mutations are statistically associated with a predicted HRD *(20)*. These data are consistent with the classification of responder for LuCaPs 141 and 141CR despite an *RB1*^{WT} genotype and lack of SLFN11 expression.

***In vivo* models of mPC validate organoid response classes to B7H3-PBD-ADC therapy**

Based on the *in vitro* B7H3-PBD-ADC response data and analysis of potential biomarkers, we evaluated the efficacy of B7H3-PBD-ADC treatment in preclinical trials of PDX models representative of different phenotype and genotype mPC categories defined by organoid studies: *RB1*^{NULL} (SLFN11^{+} or SLFN11^{-}) and *RB1*^{WT} (SLFN11^{+} or SLFN11^{-}) tumors (**Fig. 6**). We randomized mice implanted with PDX lines to treatment with two intraperitoneal doses of 1mg/kg B7H3-PBD-ADC or control R347-PBD-ADC, given weekly for two weeks. The SCNPC LuCaP 145.2 (*TP53*^{ALT}*RB1*$^{-/-}$SLFN11^{+}) line showed a complete and durable response to B7H3-PBD-ADC treatment (**Fig. 6A**). Control R347-PBD-ADC and vehicle-treated mice had similar tumor growth indicating no apparent non-specific effects of PBD at a 1 mg/kg dose. Remarkably,

no tumors were detected in 8 out of 9 B7H3-PBD-ADC treated mice 3 months after therapy. Furthermore, two of the large established tumors (>1000 mm3) were completely regressed with just two doses of B7H3-PBD-ADC (**Fig. 6A, right panel**).

Similarly, the LuCaP 136 ARPC PDX (*TP53*$^{-/-}$*RB1*$^{-/-}$SLFN11^{-}) showed complete durable response in all 6 mice treated with B7H3-PBD-ADC compared to control R347-PBD-ADC treated or vehicle treated mice (**Fig. 6B**). LuCaP 136 was not evaluable for *in vitro* responses due to poor growth characteristics beyond 1 week, but the *RB1* loss phenotype predicted *in vivo* responsiveness. Again, B7H3-PBD-ADC treatment resulted in a remarkable decrease in large tumor burden (~800 mm3) in 2 mice (**Fig. 6B, right panel**). 100% of the mice were tumor free for more than 4 months after treatment. Further, B7H3-PBD-ADC treatment of the ARPC LuCaP 77 xenograft (*RB1*^{WT}SLFN11^{+}) also showed a durable response relative to R347-PBD-ADC treated mice (**Fig. 6C**). In contrast, the ARPC LuCaP 167 xenograft (*RB1*^{WT}SLFN11^{-}) which did not respond to B7H3-PBD-ADC in vitro, also showed no significant tumor regression with B7H3-PBD-ADC treatment compared to R347-PBD-ADC treated or vehicle treated mice (**Fig. 6D**). Body weights were unaffected by the ADC in all preclinical trials (**Fig. S6, A-D**). Thus, the treatment responses assessed via organoid assays accurately predicted the *in vivo* responses to B7H3-PBD-ADC.

Because the majority of clinical mPCs progress following ADT and ARSI treatment with the retention of AR signaling, and patients often harbor bone metastases, we further tested B7H3-PBD-ADC activity against a late-stage ARPC bone metastasis model. We developed a model system whereby intracardiac injection of luciferase-tagged AR^{+} LuCaP 136 (*TP53*$^{-/-}$*RB1*$^{-/-}$ SLFN11^{-}) tumor cells colonized bone with 100% efficiency. The majority of metastases were located in the vertebrae. Other sites included calvaria, sternum, and long bones, as well as <10%

of tumor burden in soft tissue (adrenals and liver). Using bioluminescence imaging (BLI) to monitor the growth of tumor metastasis, mice were grouped into two arms of equal average metastasis burden. B7H3-PBD-ADC treatment once weekly, for two weeks, substantially reduced tumor burden resulting in no detectable metastasis compared to control R347-PBD-ADC treated mice (**Fig. 6, E and F**). Overall, B7H3-PBD-ADC treatment resulted in long-term metastasis-free survival in 100% of the treated mice (**Fig. 6G**). These data extend B7H3-PBD-ADC efficacy to tumors residing in clinically significant microenvironments.

Distribution of biomarkers in clinical samples

We related the results presented here (**Fig. 7A**) to the distribution of biomarkers in clinical CRPC by analyzing the SU2C mPC data set, considering samples with >30% tumor content (303 samples were included) (**Fig. 7B**). Within these samples ~10% demonstrated homozygous *RB1* alterations *(22, 23)*. The influence of SLFN11 upon drug sensitivity has been associated qualitatively with presence of the RNA and protein *(9, 18, 19)*. From the SU2C RNAseq data, we estimated that about 40% of *RB1* intact samples expressed SLFN11 (see methods) (**Fig. 7B**). Further, of the remaining $RB1^{WT}/SLFN11^{NEG}$ samples, about one quarter demonstrated IFN signature scores in the upper quartile. Of interest, IFN score did not appear to associate with homozygous *RB1* loss (**Fig. 7C**), but was most highly expressed in non-neuroendocrine, AR signaling low samples, a class of mPC where ADT and ARSI resistance is associated with increased plasticity (**Fig. S7, A and B**) *(24)*. In summary, considering any one biomarker as predictive for response, approximately 65% of the SU2C cohort could have been considered further for B7H3-PBD-ADC treatment pending the determination of B7H3 protein expression.

DISCUSSION

Here we evaluated a large cohort of mPC patient tumors and models representing the extensive genomic and phenotypic heterogeneity of clinical disease for responsiveness to PBD, a DNA interstrand cross-linking chemotherapeutic, delivered through a B7H3 targeted ADC. As acquired resistance to ARSIs occurs with near universal frequency, novel approaches to treatment of advanced castration resistant mPC are needed. We determined that B7H3 is expressed across a diverse spectrum of late-stage treatment-resistant metastatic mPC genotypes and phenotypes as well as across metastatic sites, which extends prior analyses of B7H3 in prostate cancer *(25, 26)*. Notably, PBD delivered via B7H3-ADC directed exposure exhibited a range of *in vitro* and *in vivo* activity against mPC organoid models that reflect the phenotypic and genotypic heterogeneity observed in patients. The molecular interrogation of these models revealed that the underlying molecular states of specific mPCs associated with response or resistance metrics. These molecular states were categorized into biomarker-defined classes of responsive models based upon: (i) B7H3 expression; (ii) pre-existing genomic vulnerabilities including replication stress and cell-autonomous IFN responses; and (iii) inability to efficiently repair PBD-initiated DNA damage. Thus, multiple vulnerabilities distinct from AR dependent survival and including but expanded beyond homologous recombination deficiencies can be exploited using PBD based therapeutics. The mPC PDX/organoid cohort analyzed here approximates the distribution of identified baseline biomarkers, such as mutations in DNA damage repair pathway components and SLFN11/interferon score expression, observed in the large SU2C CRPC clinical data set. It is anticipated that the classification and associated rationale for biomarker-identified organoids here largely reflects the potential response spectrum in clinical mPC and will inform the design of prospective trials much more accurately than prior

therapeutics analyses with limited numbers of *in vitro* growth selected mPC cell line models previously available.

Similar to the conclusions concerning antigen expression for other ADCs, the response to B7H3-PBD-ADC in a majority of the mPC organoid models was not directly related to B7H3 expression *(7, 27)*. While B7H3 expression is required, responses were also associated with other parameters including those involved directly or indirectly in the repair of PBD-initiated DNA interstrand crosslinks, a major consequence of which is the deleterious blockage of replication forks. Consistent with the synthetic lethal activity of HRD, we determined that complete loss of *CHD1* was uniquely associated with a responsive model, LuCaP 141, lacking other predictive biomarkers. On the other hand, the LuCaP 96 model, which displays loss of function for *BRCA2,* a classical HRD protein, was non-responsive to B7H3-PBD-ADCs. It should be noted that LuCaP 96 expressed WT *TP53*, and previous analyses of *BRCA1/2* deficient breast cancer PDXs have suggested approximately 25% are non-responsive to PBD, a phenotype that may be associated with a less compromised HRD resulting from minimal mutations to additional DNA repair proteins, including *TP53 (28, 29)*. Finally, it has previously been shown that inhibition of ATR, a cell cycle checkpoint protein that is crucial for allowing replication fork repair prior to entry into M phase, is a synthetic lethal for *in vitro* selected SLFN11^{NEG} tumors *(9, 19)*. We characterized a naturally occurring, PBD-responsive, SLFN11^{NEG} ATR loss of function model, NCI-PC155, consistent with these previous findings from experimentally-selected models *(19)*.

A second category of biomarkers associated with B7H3-PBD-ADC treatment involve a vulnerability to replication stress. A unique conclusion of this study is that mPCs with functional alterations in WT TP53 and RB1 are highly sensitive to the B7H3-PBD-ADC irrespective of their histological phenotype. Defects in *RB1* and *TP53* pathways are known to promote loss of

cell cycle checkpoint control, increased proliferation, and enhanced replication stress *(23)*, and additional blockage of replication forks by PBD induced ICLs likely contributes to its potent cytotoxicity. It will be useful to determine whether ADCs with PBD payloads have the potential to be efficacious in other cancer types with high replication stress phenotypes.

Autonomous interferon signatures are widely observed in various tumor types *(30)*, and there has been great interest in understanding the underlying biology. Utilizing the interferon score may have clinical utility in therapeutic applications such as responses to immune based therapeutics. In the present study of mPCs, we found that a cell-autonomous IFN score was positively correlated with the sensitivity of mPCs to B7H3-PBD-ADCs. SLFN11 is a non-canonical IFN response gene *(17)* and likely contributes to the responder phenotype as we found that SLFN11 expression is highly correlated with responsiveness to PBD. SLFN11 is a DNA/RNA helicase that is actively recruited to sites of DNA damage and appears to irreversibly block stressed replication forks, leading to the hypothesis that SLFN11 is a dominant inhibitor of stressed replication fork repair. SLFN11 is a biomarker for response to a variety of other therapeutics, including topoisomerase and PARP inhibitors as well as platinum chemotherapeutics *(9, 18)*. It is worth noting that SLFN11 protein levels are not quantitatively correlated with IFN scores (**Fig. 4B**), suggesting there may be additional factors in the interferon score phenotype that contribute to responsiveness. The predictive value of an interferon score in the context of other therapeutics that act via double stranded DNA breaks is of obvious interest as an IFN score has the potential to categorize mPCs for DNA damage dependent vulnerabilities.

In summary, B7H3-PBD-ADCs deliver a potent ICL agent with substantial anti-tumor effects toward particular subtypes of mPC. Several acquired resistance mechanisms in mPC appear sensitive to the action of PBD, supporting further evaluation as a therapeutic strategy for cancers

that are refractory to currently approved agents. Collectively, our analyses suggest that mPCs vulnerable to PBD action can be identified by a composite set of biomarkers that reflect properties of tumor phenotype (e.g. SCNPC), B7H3 expression, ongoing replication stress, HRD, and the characteristic of high interferon score, frequently associated with altered *TP53*. The approach reported here for identifying biomarkers of vulnerability to a particular cancer therapeutic using diverse models representative of clinically-relevant genotypes and phenotypes has the potential to increase the reliability of translation to the clinic, and also provide insights into mechanisms that underlie the more precise allocation of therapy.

MATERIALS AND METHODS

Study design. The objective of this study was to evaluate B7H3 expression and treatment efficacy of the B7H3 ADC armed with a pyrrolobenzodiazepine warhead (SG3315) in a diverse spectrum of PDX/organoid preclinical models of mPC. An additional objective was to identify predictive biomarkers of B7H3-PBD response. In total, 37 mPC organoid models were evaluated for B7H3 expression. At least 26 of 37 organoid models that can be grown in vitro for a minimum of 10 days were tested with the ADCs (**Fig. S3A**). Gene expression data for 24 out of 26 organoid models (not available for 23.1CR and 77CR) was utilized to identify correlates of PBD response.

For *in vivo* studies, the sample size for each experiment is indicated in the figure legend. The animal caretaker who assessed and treated animals, and measured tumors was blinded to the intervention. All other investigators were not blinded for any experiments.

RNA Sequencing Analysis of mPC tumors. RNA isolation and sequencing of 185 UW mPC tumors from 98 patients were performed as described previously *(2)* . Sequencing reads were

mapped to the hg38 human genome using STAR.v2.7.3a. All subsequent analyses were performed in R. Gene level abundance was quantitated using GenomicAlignments and transformed to $\log_2$ FPKM. Groups were compared using two-sided Wilcoxon rank tests with Benjamini-Hochberg multiple-testing correction. To evaluate the expression of B7H3 from tumors within the same patient, boxplots of transcript levels from tumors from the same patient were filtered to include only patients with at least two tumors profiled (149 tumors from 62 patients) and are ordered by per-patient median $\log_2$ FPKM gene expression.

Immunohistochemistry. Tissue microarray (TMA) slides consisting of triplicate cores from 181 metastatic prostate sites representing 58 donors was provided by the GU Lab at the University of Washington. Automated IHC was performed on the VENTANA Discovery Ultra (Ventana Medical Systems Inc) autostainer. Onboard deparaffinization was conducted in DISCOVERY Wash buffer (VMSI, 950-510). Subsequent heat-induced epitope retrieval (HIER) was performed in DISCOVERY CC1 solution (VMSI, 950-500). Tissue microarray sections were incubated with B7H3 recombinant rabbit monoclonal antibody (Sigma Aldrich, SP206) at a dilution of 1:500 in Ventana Antibody Diluent with Casein (VMSI, 760-219). The primary antibody was bound with DISCOVERY anti-Rabbit HQ secondary antibody (Ventana), followed by DISCOVERY Anti-HQ HRP (VMSI, 760-4820) enzyme conjugate. The antibody complex was visualized using the ChromoMap DAB detection Kit (VMSI, Cat# 760-159). Hematoxylin II (VMSI, 790-2208) and Bluing Reagent (VMSI, 760-2037) were used to counterstain the sections.

The TMA slides were scanned at a 40X magnification using the Ventana DP 200 instrument (VMSI) and visualized with HALO (Indica Labs). Staining intensity was evaluated by a pathologist (M.R.). The H-score was determined by multiplying the percentage of positive cells

at each intensity level (0 denotes no staining, 1 denotes weak staining, moderate denotes staining and 3 is strong staining) by its respective intensity level. The weighted scores were totaled, resulting in a composite score ranging from 0-300. The triplicate scores for each site were averaged to generate an averaged H-score for each site.

Organoid culture. LuCaP PDX tissue samples were processed into single cells, depleted for mouse cells using mouse cell depletion kit (Miltenyi Biotec, manufacturer's protocol), and plated as organoids according to our previously described methods *(16)*. Organoids were grown in 5% Matrigel on ultra-low attachment plates/dishes (Corning) for short-term drug treatment and flow cytometry analysis. Previously defined organoid culture media *(16)* was supplemented with 5ng/ml Neuregulin 1 (Peprotech, 100-03) to potentiate the growth of adenocarcinoma organoid models.

Pharmacological agents. Two batches of antibody drug conjugates (B7H3-PBD or R347-PBD) were received from AstraZeneca. Organoid responses with an individual batch of the ADC are shown in Figure S3A. No major difference in drug response was observed. The R347 is a control human IgG1 antibody that does not bind human proteins and serves as the isotype control antibody drug conjugate. Topotecan (S9321), ATR inhibitor, Berzosertib (S7102), Carboplatin (S1215), Cisplatin (S1166), Mitomycin C (S8146), and Doxorubicin (S1208) were purchased from Selleckchem.

Organoid drug response assays. PDX tumors and organoids were dissociated into single cells, mixed with Matrigel, and plated at 1000 cells/well in 384 well poly-d-lysine coated plates (Corning). Drugs were serially diluted in organoid culture media and a total volume of 30 ul per well was added. Organoids were treated with the small molecule inhibitors, B7H3-PBD or R347-PBD (control ADC) three times for 10 days (**Fig. 3A**). Thereafter, cell viability was quantified

with CellTiter Glo 3D. Luminescence was measured using Infinite M200 Pro microplate reader (Tecan). Each experiment included five replicates. All treatments were repeated in two or more biologically independent experiments. Normalized AUC (nAUC) was calculated for each experiment as a ratio of AUC for B7H3-PBD and R347-PBD dose-response curves. Median nAUC and interquartile range was then calculated across independent experiments for each organoid model. Median nAUC was used for all further analysis. GraphPad Prism 9 was used to calculate IC_{50} and maximum drug effect (MaxR) which is shown as % viable cells at the highest concentration of 4ug/ml.

Simple Western Protein quantification. LuCaP PDXs' tissue lysates were prepared using RIPA buffer containing protease and phosphatase inhibitors. Protein samples were separated based on size using a capillary-based automated protein analysis system (Protein Simple Western Technology, Peggy Sue). Protein separation, immunodetection, and analysis steps were performed automatically by the protein analysis system. Protein bands were analyzed with the Compass software. The observed band size of B7H3 protein was variable between 120-150 kDa. GAPDH was used as the internal control. The B7H3 protein was quantified by normalizing B7H3 band intensity to the housekeeping protein, GAPDH. For the figures, the values were scaled by a factor of 10. See supplementary methods for additional details.

Immunoblots. LuCaP PDXs' tissue lysates were prepared as above. Organoid pellets were lysed in warm 1% SDS buffer with protease and phosphatase inhibitors. To shear the released DNA/RNA and reduce sample viscosity, 25 U/ul Benzonase nuclease (Sigma, E1014) was added per sample. The samples were incubated at 37 degrees for 30 minutes. Samples were then sonicated to shear leftover DNA using Bioruptor® Pico sonication system (Diogenode, sonication cycle: 30 sec ON/30 sec OFF, total sonication time: 5 cycles, temperature: 4 C).

Protein concentration was determined by BCA assay (ThermoFisher, 23225). 10-15 ug of protein lysates were run on 4–20% Criterion™ TGX™ Precast Midi Protein Gel (Bio-Rad) and then transferred to polyvinylidene difluoride membranes. Membranes were blocked in TBS with 0.1% Tween-20, 5% blotting grade blocker (Bio-Rad, 1706404XTU). The primary antibodies used are listed in Table S1. Clarity or Clarity Max™ Western ECL Substrate (Bio-Rad 1705061, 1705062S) was used for imaging the blots**.** Blots were imaged on Bio-Rad ChemiDoc Touch Imaging System.

Flow cytometry. For B7H3 cell surface expression analysis, organoids were first dissociated into single cells using Accutase (STEMCELL Technologies, 07922). The resulting single cells were resuspended in PBS and stained with 1:1000 Zombie Violet™ dye (Biolegend, 423113) for 15 minutes to exclude dead cells. Cells were pelleted and resuspended in 100 ul staining buffer (BioLegend, 420201). Fc receptors were blocked using Human TruStain FcX™ blocking solution (BioLegend, 422301) for 5 min at room temperature. Thereafter, cells were stained with human-EpCAM-APC (Miltenyi Biotec, 130-113-260) and CD276-PE (BioLegend, 331606) for 20 min at 4°C. The stained cells were washed, fixed in 4% paraformaldehyde for 10 mins, and stored in staining buffer at 4°C up to 3-5 days. Flow cytometric analysis was done on BD LSR Fortessa cell analyzer using the BD FACSDiva software. Unstained cells and cells stained with isotype control-PE/APC antibodies were used for gating live cells and the false-positive peak, respectively. Median Fluorescent intensity(MFI) and % positive cells were analyzed using FlowJo software. % Positive cells were calculated by Overton cumulative histogram subtraction algorithm in Flowjo.

Cell sorting was performed on FACSAria cell sorter (Becton Dickinson) using FACSDiva software.

IF staining. Organoids were dissociated and plated in 200 ul culture media (+/- doxycycline) with 2% Matrigel on poly-d-lysine coated chamber slides (Ibidi, 81201). After 24 hours, cells were fixed in 4% paraformaldehyde for 10 mins and stained with RB1 antibody and DAPI. Images were taken with Zeiss Axioscan.Z1 slide scanner.

CRISPR/Cas9 experiments. We used three organoid models for CRISPR experiments: LuCaP 145.2, LuCaP 173.1, and NCI-PC155. Two vector system (lentiCas9-Blast, lentiGuide-Puro) was used. First, Cas9 expressing organoid lines were generated by lentiviral transduction of Cas9 plasmid (lentiCas9-Blast, addgene; 52962) and selection with Blasticidin for 10-14 days. Individual sgRNAs were cloned into lentiGuide-Puro plasmid (NCI core facility). Cas9 expressing organoids were then transduced with lentiviral sgRNA (sgB7H3 #1; CAACCGCACGGCCCTCTTCCCGG) and selected with 1 ug/ml puromycin for 3 days. All lentiviral transductions were done by spin infection at 1000 x g, for 90 mins at 32ºC.

Since clonal culture was not possible from organoids, B7H3 sgRNA transduced LuCaP 145.2 organoids were processed into single cells and FACS sorted to enrich for B7H3 knockout cells. For later experiments, FACS sorted B7H3-WT and B7H3-KO cells were maintained in 3D organoid cultures. B7H3 knockdown was periodically confirmed by western blotting.

Details of the CRISPR/Cas9 dropout screen are provided in supplementary methods.

Preclinical trials. All animal procedures were approved by NCI Animal Care and Use Committee. Male NSG mice were subcutaneously injected with 2 million processed LuCaP PDX tumor cells or implanted with tumor pieces. When tumor exceeded ~150 mm3, mice were randomized into three groups - B7H3-PBD, R347-PBD, and vehicle. 1mg/kg of the B7H3-PBD or R347-PBD was administered intraperitoneally weekly, for two weeks. Tumor growth (mm^3) and body weight were measured twice a week. Tumor growth is shown for the individual mouse

from the time of first treatment. Mice were euthanized if any of the two tumor diameters reached 2cm or if their health was compromised.

For establishing LuCaP 136 metastasis model, processed PDX cells were first transduced with a luciferase reporter plasmid and re-injected subcutaneously in NSG mouse. The resulting tumor was processed, and 100,000 single cells were injected intracardiacally. Tumor growth was measured by bioluminescence imaging. Treatment was started when the luminescence signal reached ~3 x 10^7.

Organoid derived xenografts. Organoid derived xenografts (ODXs) were established in NOD scid gamma (NSG) mice as previously described *(16)*. The subsequent subcutaneous tumor was collected, processed and 1-2 million cells, mixed with Matrigel in 1:1 ratio, were injected subcutaneously per mice for the experiment. Mice were randomized into three treatment groups (B7H3-PBD, R347-PBD, and vehicle) when the tumors reached an average volume of 250-300 mm^3. The treatment was started as described above.

RNA-sequencing. RNA-seq was performed on the mPC organoid models on Illumina NovaSeq_S2 Flowcells using rRNA-depleted RNA and paired-end reads. Data were preprocessed and filtered using our previously described pipeline *(16)*. RNA sequence reads were aligned with STAR to the human genome, hg19. The featureCounts program from the subread package was applied to compute the raw reads count. All further analysis was performed in R. Data were TMM normalized to convert the raw read count to $\log_2$ transformed CPM (counts per million) using EdgeR. Median gene expression values were used for the biological replicates. Normalized $\log_2$CPM values were used for all subsequent analyses.

ConsensusDE package was used to perform differential expression analysis with three different algorithms (EdgeR, DESeq, and Voom) simultaneously. Genes were considered

differentially expressed if adjusted Benjamin-Hochberg false discovery rate (FDR) was less than 0.05 for all three methods.

Gene signature scores. Single sample gene set signature scores were calculated using GSVA with default parameters *(31)*, using all MSigDB gene sets and interferon signature score (IFN score) refined for prostate cancer. Gene signature scores (IFN score, Replication stress score, AR score, and RB score) used in this study are described in detail in the supplementary methods.

Clinical sample analyses. SU2C/PCF 2019 data was downloaded from cbioportal *(22)*. Log_2(FPKM+1) mean centered data was used. Since PolyA and capture sequenced RNAseq data are highly concordant *(23)*, we merged the two datasets to have unique 328 samples. Samples with at least 30% tumor content (n = 303/328) were kept for analysis. Cbioportal data was merged with curations of the *TP53/RB1* status and AR/NE state from Nyquist et al 2020 *(23)*. IFN score and RB1 score were calculated using GSVA with method argument as "ssgsea" *(31)*. For analysis of *SLFN11* status, data was normalized using ordered quantile normalization with the orderNorm function in R.

Statistical analyses. R package, ggpubr, and GraphPad Prism were used for all analyses. Pearson's correlation coefficient was calculated for scatterplots using ggscatter function in R. The nonparametric Kruskal Wallis test was used to compare multiple groups. For pairwise comparison between groups, Wilcoxon test was used with *P* value adjusted for multiple testing using the Holm method. Differences were considered significant for two-tailed *P* values of < 0.05. For correlation analysis, Benjamini and Hochberg method was applied for multiple hypothesis test correction with adjusted *P* value (FDR) ≤ 0.05 indicating statistical significance.

For in vivo metastasis experiment, treatment response was compared using GraphPad Prism by two-way Anova. Kaplan-Meier survival analysis was performed, and the survival rate

was compared by Log-rank test. Data are expressed as the mean ± SEM, with $P < 0.05$ considered statistically significant.

Heatmap was generated by using the R package ComplexHeatmap.

Supplementary Materials

Materials and Methods

Simple Western protein quantification details

CRISPR/Cas9 dropout screen

Gene signature scores

Fig. S1. B7H3 expression is mPC patient samples, PDXs, and organoids.

Fig. S2. B7H3 FACS analysis and correlation of B7H3 expression and AR score.

Fig. S3. B7H3-PBD response in organoid models and B7H3 knockout assays.

Fig. S4. Biomarker analysis of B7H3-PBD response.

Fig. S5. Assay for ATR activity in selected organoids following treatment with chemotherapeutics.

Fig. S6. Body weight for mice treated with B7H3-PBD, R347-PBD or vehicle.

Fig. S7. IFN- and RB scores for SU2C/PCF 2019 clinical samples.

Table S1. List of antibodies.

Data file S1. Descriptive data for B7H3-PBD response in 26 organoid models.

Data file S2. Differentially expressed genes between responder and Non-responder ARPC models.

References and Notes

1. R. L. Siegel, K. D. Miller, A. Jemal, Cancer statistics, 2020, *CA. Cancer J. Clin.* **70**, 7–30 (2020).

2. M. P. Labrecque, I. M. Coleman, L. G. Brown, L. D. True, L. Kollath, B. Lakely, H. M. Nguyen, Y. C. Yang, R. M. G. Da Costa, A. Kaipainen, R. Coleman, C. S. Higano, E. Y. Yu, H. H. Cheng, E. A. Mostaghel, B. Montgomery, M. T. Schweizer, A. C. Hsieh, D. W. Lin, E. Corey, P. S. Nelson, C. Morrissey, Molecular profiling stratifies diverse phenotypes of treatment-refractory metastatic castration-resistant prostate cancer, *J. Clin. Invest.* **129**, 4492–4505 (2019).

3. O. Sartor, J. de Bono, K. N. Chi, K. Fizazi, K. Herrmann, K. Rahbar, S. T. Tagawa, L. T. Nordquist, N. Vaishampayan, G. El-Haddad, C. H. Park, T. M. Beer, A. Armour, W. J. Pérez-Contreras, M. DeSilvio, E. Kpamegan, G. Gericke, R. A. Messmann, M. J. Morris, B. J. Krause, Lutetium-177–PSMA-617 for Metastatic Castration-Resistant Prostate Cancer, *N. Engl. J. Med.* **385**, 1091–1103 (2021).

4. M. E. Goebeler, R. C. Bargou, T cell-engaging therapies — BiTEs and beyond, *Nat. Rev. Clin. Oncol.* **17**, 418–434 (2020).

5. T. B. Dorff, V. Narayan, S. J. Forman, P. D. Zang, J. A. Fraietta, C. H. June, N. B. Haas, S. J. Priceman, Novel Redirected T-Cell Immunotherapies for Advanced Prostate Cancer, *Clin. Cancer Res.* **28**, 576–584 (2022).

6. M. Rosellini, M. Santoni, V. Mollica, A. Rizzo, A. Cimadamore, M. Scarpelli, N. Storti, N. Battelli, R. Montironi, F. Massari, Treating prostate cancer by antibody-drug conjugates, *Int. J. Mol. Sci.* **22**, 1–15 (2021).

7. K. Tsuchikama, Z. An, Antibody-drug conjugates: recent advances in conjugation and linker chemistries, *Protein Cell* **9**, 33–46 (2018).

8. J. A. Hartley, Antibody-drug conjugates (ADCs) delivering pyrrolobenzodiazepine (PBD) dimers for cancer therapy, *Expert Opin. Biol. Ther.* **21**, 931–943 (2021).

9. U. Jo, Y. Murai, N. Takebe, A. Thomas, Y. Pommier, Precision oncology with drugs targeting the replication stress, ATR, and schlafen 11*Cancers (Basel).* **13**, 1–22 (2021).

10. T. Ubhi, G. W. Brown, Exploiting DNA replication stress for cancer treatment, *Cancer Res.* **79**, 1730–1739 (2019).

11. K. Flem-Karlsen, Ø. Fodstad, M. Tan, C. E. Nunes-Xavier, B7-H3 in Cancer – Beyond Immune Regulation, *Trends in Cancer* **4**, 401–404 (2018).

12. E. Picarda, K. C. Ohaegbulam, X. Zang, Molecular pathways: Targeting B7-H3 (CD276) for human cancer immunotherapy, *Clin. Cancer Res.* **22**, 3425–3431 (2016).

13. F. Kontos, T. Michelakos, T. Kurokawa, A. Sadagopan, J. H. Schwab, C. R. Ferrone, S. Ferrone, B7-H3: An attractive target for antibody-based immunotherapy, *Clin. Cancer Res.* **27**, 1227–1235 (2021).

14. S. Seaman, Z. Zhu, S. Saha, X. M. Zhang, M. Y. Yang, M. B. Hilton, K. Morris, C. Szot, H. Morris, D. A. Swing, L. Tessarollo, S. W. Smith, S. Degrado, D. Borkin, N. Jain, J. Scheiermann, Y. Feng, Y. Wang, J. Li, D. Welsch, G. DeCrescenzo, A. Chaudhary, E. Zudaire,

K. D. Klarmann, J. R. Keller, D. S. Dimitrov, B. St. Croix, Eradication of Tumors through Simultaneous Ablation of CD276/B7-H3-Positive Tumor Cells and Tumor Vasculature, *Cancer Cell* **31**, 501-515.e8 (2017).

15. H. M. Nguyen, R. L. Vessella, C. Morrissey, L. G. Brown, I. M. Coleman, C. S. Higano, E. A. Mostaghel, X. Zhang, L. D. True, H. M. Lam, M. Roudier, P. H. Lange, P. S. Nelson, E. Corey, LuCaP Prostate Cancer Patient-Derived Xenografts Reflect the Molecular Heterogeneity of Advanced Disease an--d Serve as Models for Evaluating Cancer Therapeutics, *Prostate* **77**, 654–671 (2017).

16. M. L. Beshiri, C. M. Tice, C. Tran, H. M. Nguyen, A. G. Sowalsky, S. Agarwal, K. H. Jansson, Q. Yang, K. M. McGowen, J. J. Yin, A. N. Alilin, F. H. Karzai, W. L. Dahut, E. Corey, K. Kelly, A PDX/Organoid biobank of advanced prostate cancers captures genomic and phenotypic heterogeneity for disease modeling and therapeutic screening, *Clin. Cancer Res.* **24**, 4332–4345 (2018).

17. Y. Murai, U. Jo, J. Murai, S. Fukuda, N. Takebe, Y. Pommier, Schlafen 11 expression in human acute leukemia cells with gain-of-function mutations in the interferon-JAK signaling pathway, *iScience* **24**, 103173 (2021).

18. G. Zoppoli, M. Regairaz, E. Leo, W. C. Reinhold, S. Varma, A. Ballestrero, J. H. Doroshow, Y. Pommier, Putative DNA/RNA helicase Schlafen-11 (SLFN11) sensitizes cancer cells to DNA-damaging agents, *Proc. Natl. Acad. Sci. U. S. A.* **109**, 15030–15035 (2012).

19. S. Mao, R. Chaerkady, W. Yu, G. D'Angelo, A. Garcia, H. Chen, A. M. Barrett, S. Phipps, R. Fleming, S. Hess, J. O. Koopmann, N. Dimasi, S. Wilson, K. Pugh, K. Cook, L. A. Masterson, C. Gao, H. Wu, R. Herbst, P. W. Howard, D. A. Tice, M. Cobbold, J. Harper, Resistance to pyrrolobenzodiazepine dimers is associated with SLFN11 downregulation and can be reversed through inhibition of ATR, *Mol. Cancer Ther.* **20**, 541–552 (2021).

20. N. De Sarkar, S. Dasgupta, P. Chatterjee, I. Coleman, G. Ha, L. S. Ang, E. A. Kohlbrenner, S. B. Frank, T. A. Nunez, S. J. Salipante, E. Corey, C. Morrissey, E. Van Allen, M. T. Schweizer, M. C. Haffner, R. Patel, B. Hanratty, J. M. Lucas, R. F. Dumpit, C. C. Pritchard, R. B. Montgomery, P. S. Nelson, Genomic attributes of homology-directed DNA repair deficiency in metastatic prostate cancer, *JCI Insight* **6** (2021), doi:10.1172/jci.insight.152789.

21. V. Kari, W. Y. Mansour, S. K. Raul, S. J. Baumgart, A. Mund, M. Grade, H. Sirma, R. Simon, H. Will, M. Dobbelstein, E. Dikomey, S. A. Johnsen, Loss of CHD 1 causes DNA repair defects and enhances prostate cancer therapeutic responsiveness , *EMBO Rep.* **19**, 1609–1623 (2018).

22. W. Abida, J. Cyrta, G. Heller, D. Prandi, J. Armenia, I. Coleman, M. Cieslik, M. Benelli, D. Robinson, E. M. Van Allen, A. Sboner, T. Fedrizzi, J. M. Mosquera, B. D. Robinson, N. De Sarkar, L. P. Kunju, S. Tomlins, Y. M. Wu, D. N. Rodrigues, M. Loda, A. Gopalan, V. E. Reuter, C. C. Pritchard, J. Mateo, D. Bianchini, S. Miranda, S. Carreira, P. Rescigno, J. Filipenko, J. Vinson, R. B. Montgomery, H. Beltran, E. I. Heath, H. I. Scher, P. W. Kantoff, M. E. Taplin, N. Schultz, J. S. Debono, F. Demichelis, P. S. Nelson, M. A. Rubin, A. M. Chinnaiyan, C. L. Sawyers, Genomic correlates of clinical outcome in advanced prostate cancer, *Proc. Natl. Acad. Sci. U. S. A.* **166**, 11428–11436 (2019).

23. M. D. Nyquist, A. Corella, I. Coleman, N. De Sarkar, A. Kaipainen, G. Ha, R. Gulati, L. Ang, P. Chatterjee, J. Lucas, C. Pritchard, G. Risbridger, J. Isaacs, B. Montgomery, C.

Morrissey, E. Corey, P. S. Nelson, Combined TP53 and RB1 Loss Promotes Prostate Cancer Resistance to a Spectrum of Therapeutics and Confers Vulnerability to Replication Stress., *Cell Rep.* **31**, 107669 (2020).

24. S. Laudato, A. Aparicio, F. G. Giancotti, Clonal Evolution and Epithelial Plasticity in the Emergence of AR-Independent Prostate Carcinoma, *Trends in Cancer* **5**, 440–455 (2019).

25. L. Brady, M. Kriner, I. Coleman, C. Morrissey, M. Roudier, L. D. True, R. Gulati, S. R. Plymate, Z. Zhou, B. Birditt, R. Meredith, G. Geiss, M. Hoang, J. Beechem, P. S. Nelson, Inter- and intra-tumor heterogeneity of metastatic prostate cancer determined by digital spatial gene expression profiling, *Nat. Commun.* **12**, 1–16 (2021).

26. B. Benzon, S. G. Zhao, M. C. Haffner, M. Takhar, N. Erho, K. Yousefi, P. Hurley, J. L. Bishop, J. Tosoian, K. Ghabili, M. Alshalalfa, S. Glavaris, B. W. Simons, P. Tran, E. Davicioni, R. J. Karnes, K. Boudadi, E. S. Antonarakis, E. M. Schaeffer, C. G. Drake, F. Feng, A. E. Ross, Correlation of B7-H3 with androgen receptor, immune pathways and poor outcome in prostate cancer: An expression-based analysis, *Prostate Cancer Prostatic Dis.* **20**, 28–35 (2017).

27. N. M. Kendsersky, J. Lindsay, E. Anders Kolb, M. A. Smith, B. A. Teicher, S. W. Erickson, E. J. Earley, Y. P. Mosse, D. Martinez, J. Pogoriler, K. Krytska, K. Patel, D. Groff, M. Tsang, S. Ghilu, Y. Wang, S. Seaman, Y. Feng, B. St Croix, R. Gorlick, R. Kurmasheva, P. J. Houghton, J. M. Maris, The B7-H3–targeting antibody–Drug conjugate m276-SL-PBD is potently effective against pediatric cancer preclinical solid tumor models, *Clin. Cancer Res.* **27**, 2938–2946 (2021).

28. K. N. Maxwell, B. Wubbenhorst, B. M. Wenz, D. De Sloover, J. Pluta, L. Emery, A. Barrett, A. A. Kraya, I. N. Anastopoulos, S. Yu, Y. Jiang, H. Chen, N. R. Zhang, N. Hackman, K. D'Andrea, R. Daber, J. J. D. Morrissette, N. Mitra, M. Feldman, S. M. Domchek, K. L. Nathanson, BRCA locus-specific loss of heterozygosity in germline BRCA1 and BRCA2 carriers, *Nat. Commun.* **8**, 1–11 (2017).

29. H. Zhong, C. Chen, R. Tammali, S. Breen, J. Zhang, C. Fazenbaker, M. Kennedy, J. Conway, B. W. Higgs, N. Holoweckyj, R. Raja, J. Harper, A. J. Pierce, R. Herbst, D. A. Tice, Improved therapeutic window in BRCA-mutant tumors with antibody-linked pyrrolobenzodiazepine dimers with and without PARP inhibition, *Mol. Cancer Ther.* **18**, 89–99 (2019).

30. R. R. Weichselbaum, H. Ishwaran, T. Yoon, D. S. a Nuyten, S. W. Baker, N. Khodarev, A. W. Su, A. Y. Shaikh, P. Roach, B. Kreike, B. Roizman, J. Bergh, Y. Pawitan, M. J. van de Vijver, A. J. Minn, An interferon-related gene signature for DNA damage resistance is a predictive marker for chemotherapy and radiation for breast cancer., *Proc. Natl. Acad. Sci. U. S. A.* **105**, 18490–18495 (2008).

31. S. Hänzelmann, R. Castelo, J. Guinney, GSVA: Gene set variation analysis for microarray and RNA-Seq data, *BMC Bioinformatics* **14** (2013), doi:10.1186/1471-2105-14-7.

32. S. B. Dreyer, R. Upstill-Goddard, V. Paulus-Hock, C. Paris, E. M. Lampraki, E. Dray, B. Serrels, G. Caligiuri, S. Rebus, D. Plenker, Z. Galluzzo, H. Brunton, R. Cunningham, M. Tesson, C. Nourse, U. M. Bailey, M. D. Jones, K. Moran-Jones, D. W. Wright, F. Duthie, K. Oien, L. Evers, C. J. McKay, G. A. McGregor, A. Gulati, R. Brough, I. Bajrami, S. Pettitt, M. L. Dziubinski, J. Candido, F. Balkwill, S. T. Barry, R. Grützmann, L. Rahib, S. Allison, P. J. Bailey, A. V. Biankin, D. Beraldi, E. Cameron, D. K. Chang, S. L. Cooke, P. Grimwood, S. Kelly, J. Marshall, S. Martin, B. McDade, D. McElroy, E. A. Musgrove, D. Ramsay, D. Wright,

J. Hair, N. B. Jamieson, P. Westwood, N. Williams, A. L. Johns, A. Mawson, C. J. Scarlett, M. A. L. Brancato, S. J. Rowe, S. H. Simpson, M. Martyn-Smith, M. T. Thomas, L. A. Chantrill, V. T. Chin, A. Chou, M. J. Cowley, J. L. Humphris, R. S. Mead, A. M. Nagrial, M. Pajic, J. Pettit, M. Pinese, I. Rooman, J. Wu, J. Tao, R. DiPietro, C. Watson, A. Steinmann, H. C. Lee, R. Wong, A. V. Pinho, M. Giry-Laterriere, R. J. Daly, R. L. Sutherland, S. M. Grimmond, N. Waddell, K. S. Kassahn, D. K. Miller, P. J. Wilson, A. M. Patch, S. Song, I. Harliwong, S. Idrisoglu, E. Nourbakhsh, S. Manning, S. Wani, M. Gongora, M. Anderson, O. Holmes, C. Leonard, D. Taylor, S. Wood, C. Xu, K. Nones, J. L. Fink, A. Christ, T. Bruxner, N. Cloonan, F. Newell, J. V. Pearson, M. Quinn, S. Nagaraj, S. Kazakoff, N. Waddell, K. Krisnan, K. Quek, D. Wood, J. S. Samra, A. J. Gill, N. Pavlakis, A. Guminski, C. Toon, R. Asghari, N. D. Merrett, D. Pavey, A. Das, P. H. Cosman, K. Ismail, C. O'Connnor, V. W. Lam, D. McLeod, H. C. Pleass, A. Richardson, V. James, J. G. Kench, C. L. Cooper, D. Joseph, C. Sandroussi, M. Crawford, J. Gallagher, M. Texler, C. Forest, A. Laycock, K. P. Epari, M. Ballal, D. R. Fletcher, S. Mukhedkar, N. A. Spry, B. DeBoer, M. Chai, N. Zeps, M. Beilin, K. Feeney, N. Q. Nguyen, A. R. Ruszkiewicz, C. Worthley, C. P. Tan, T. Debrencini, J. Chen, M. E. Brooke-Smith, V. Papangelis, H. Tang, A. P. Barbour, A. D. Clouston, P. Martin, T. J. O'Rourke, A. Chiang, J. W. Fawcett, K. Slater, S. Yeung, M. Hatzifotis, P. Hodgkinson, C. Christophi, M. Nikfarjam, A. Mountain, V. C. Biobank, J. R. Eshleman, R. H. Hruban, A. Maitra, C. A. Iacobuzio-Donahue, R. D. Schulick, C. L. Wolfgang, R. A. Morgan, M. Hodgin, A. Scarpa, R. T. Lawlor, S. Beghelli, V. Corbo, M. Scardoni, C. Bassi, M. A. Tempero, J. S. Graham, F. E. M. Froeling, P. Beer, G. M. Petersen, A. Ashworth, M. C. Frame, H. C. Crawford, D. M. Simeone, C. Lord, D. Mukhopadhyay, C. Pilarsky, D. A. Tuveson, J. P. Morton, O. J. Sansom, Targeting DNA Damage Response and Replication Stress in Pancreatic Cancer, *Gastroenterology* **160**, 362-377.e13 (2021).

33. P. G. Febbo, P. Mendiratta, E. Mostaghel, J. Guinney, A. K. Tewari, A. Porrello, W. T. Barry, P. S. Nelson, Genomic strategy for targeting therapy in castration-resistant prostate cancer, *J. Clin. Oncol.* **27**, 2022–2029 (2009).

34. C. McNair, K. Xu, A. C. Mandigo, M. Benelli, B. Leiby, D. Rodrigues, J. Lindberg, H. Gronberg, M. Crespo, B. De Laere, L. Dirix, T. Visakorpi, F. Li, F. Y. Feng, J. De Bono, F. Demichelis, M. A. Rubin, M. Brown, K. E. Knudsen, Differential impact of RB status on E2F1 reprogramming in human cancer, *J. Clin. Invest.* **128**, 341–358 (2018).

Acknowledgments:

The authors wish to express their gratitude to the patients and the families of the patients who contributed to this study. We thank Yves Pommier for reviewing the manuscript. We also thank all the NCI/CCR core facilities including LGCP microscopy core, Flow cytometry core for assistance with cell sorting, Genomics core for performing RNA sequencing, Genome Modification core for designing CRISPR guides, and Nanoscale Protein Analysis Section of the CCR Collaborative Protein Technology Resource for performing Simple Western assays. We gratefully acknowledge support for this study from The Richard Lucas Foundation, The Prostate Cancer Foundation, NIH PO1 CA163227, the PNW Prostate Cancer SPORE NIH P50 CA097186, PC200262, and the Department of Defense Prostate Cancer Research Program W81XWH-14-2-0183.

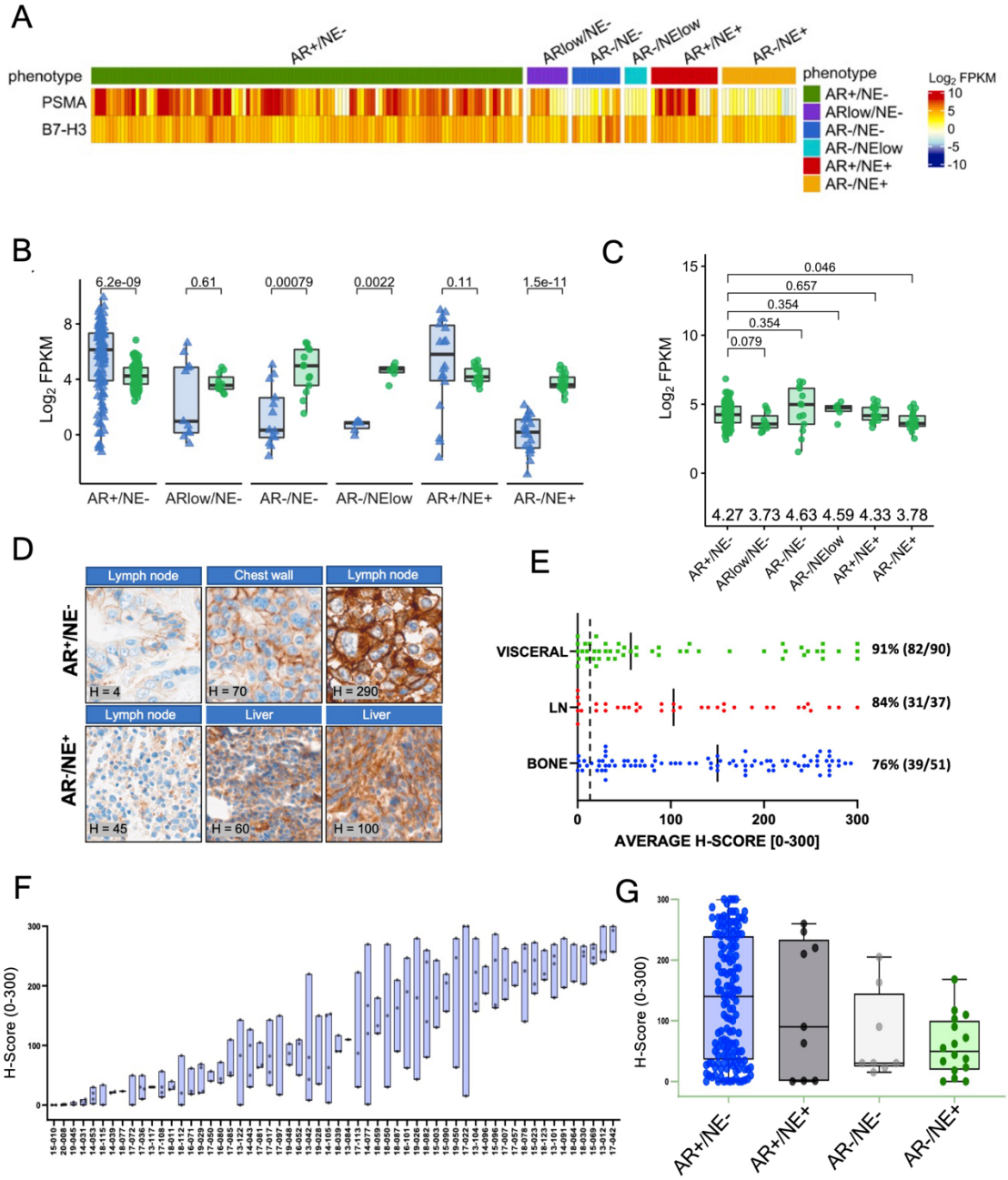

FIG. 1. CD276/B7H3 expression in metastatic prostate cancer. **(A)** CD276/B7H3 and

PSMA/FOLH1 transcript abundance determined by RNA sequencing analysis of 185 metastatic prostate tumors from 98 patients. Transcript levels are shown as Log2 FPKM. **(B)** Comparisons of B7H3 and PSMA expression by phenotypes of metastatic tumors. Groups were compared using two-sided Wilcoxon rank tests with Benjamini-Hochberg multiple-testing correction. **(C)** Data from panel B plotted to show statistical comparisons of B7H3 across mPC phenotypes. **(D)** Immunohistochemical assessments of B7H3 protein expression. Representative staining of tumors with low, medium and high B7H3 expression in AR+/NE- and AR-/NE+ phenotypes. **(E)** Distribution of B7H3 protein expression in metastatic tumors from different sites. Dashed line shows H-score of 20. Solid line shows the mean H-score. **(F)** Distribution of B7H3 protein expression in 181 metastatic tumors within and between 58 patients. **(G)** Distribution of B7H3 protein expression in metastatic prostate cancers categorized by phenotype.

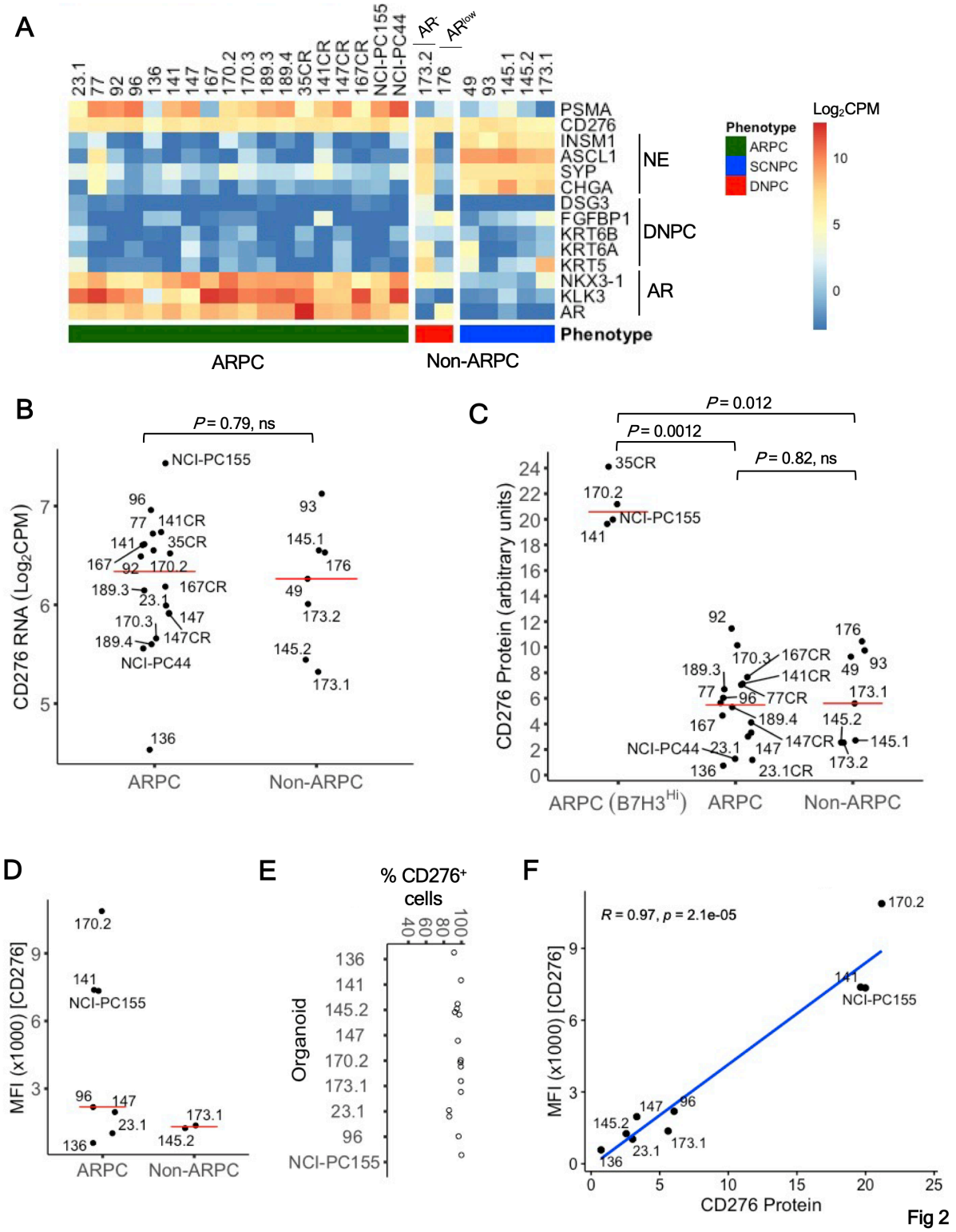

FIG. 2. B7H3 (CD276) expression in mPC PDX and organoid models. (A) Molecular profile

of organoid models tested in this study based on AR-, DNPC-, and neuroendocrine (NE) associated genes. B7H3 and PSMA/FOLH1 transcript levels are shown as Log_2CPM. ARPC = AR-active adenocarcinoma (Intact and experimentally castrate resistant), Non-ARPC = SCNPC (LuCaPs 49, 93, 145.1, 145.2, 173.1) and $AR^{NEG/LOW}$ NE^{NEG} (LuCaPs 173.2 and 176, respectively, grouped as DNPC) *(2)* phenotypes. Transcript data not available for 23.1CR and 77CR organoids. **(B)** Dot plot for B7H3 RNA expression in mPC organoids based on phenotypes. The red line indicates median B7H3 expression. **(C)** Western blot quantification of B7H3 protein expression in PDX tissue samples and two PDOs (NCI-PC44, NCI-PC155) by Simple Western. ARPC samples with high B7H3 expression are categorized separately in the $B7H3^{HI}$ group. Y-axis represents CD276 protein quantification scaled by a factor of 10. ns = not significant. **(D-E)** Flow cytometry analysis for B7H3 cell-surface expression from organoids dissociated into single cells. **(D)** Median Fluorescence Intensity (MFI) and **(E)** % positive cells are shown for nine analyzed models. **(F)** Scatter plot for Pearson correlation between B7H3 cell surface expression by flow cytometry (MFI) and total protein expression by Simple Western.

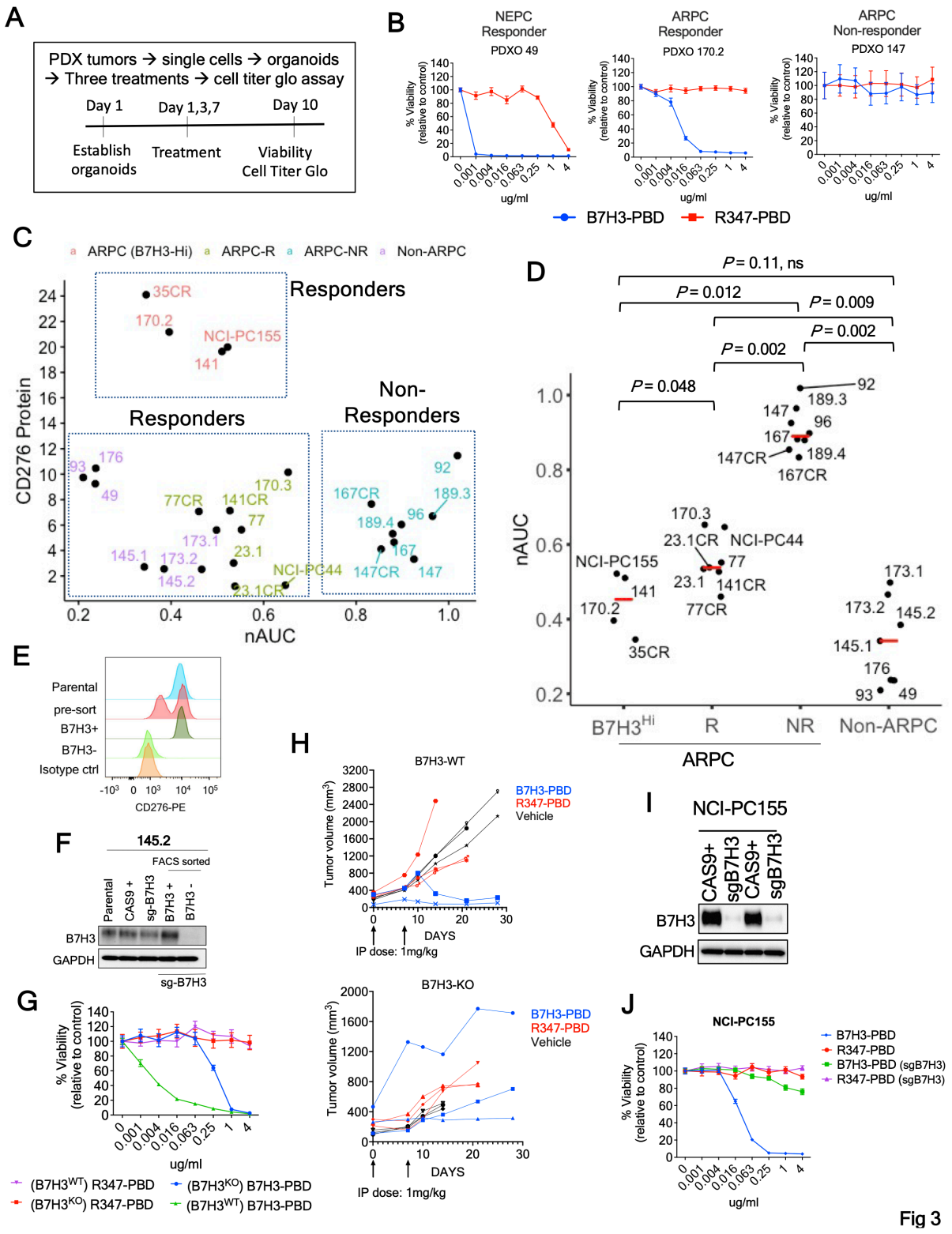

FIG. 3. B7H3-PBD-ADC activity requires, but is not correlated with, B7H3 expression

levels. (A) Schematic of the ex-vivo drug assay. **(B)** Representative drug response curves for B7H3-PBD-ADC and R347-PBD-ADC (control ADC) in PDXOs of SCNPC and ARPC phenotypes. % Viability was plotted relative to the control. **(C)** Comparison of B7H3-PBD-ADC response and B7H3 protein expression across the models; n=26. **(D)** Normalized AUC (nAUC) values for B7H3-PBD-ADC in ARPC (n=19) and non-ARPC models (n=7). ARPC models are categorized into three groups: high B7H3 expressors ($B7H3^{HI}$) n=4, responder (R) n=7, and non-Responder (NR) n = 8. Red line indicates median nAUC for the groups. **(E)** FACS sorting strategy for selecting B7H3-KO 145.2 cells. **(F)** Western blot for FACS sorted 145.2 $B7H3^{+}$ and $B7H3^{-}$ (B7H3-KO) cells grown as organoids. **(G)** Dose response curves for 145.2 B7H3-KO and B7H3-WT organoids treated with ADC for 10 days. **(H)** 145.2 B7H3-WT (top) and B7H3-KO (bottom) ODXs treated with ADCs or vehicle, weekly for two weeks, as indicated by arrows; n = 3/group, except B7H3-KO (vehicle group; n=2) and B7H3-WT (B7H3-PBD group; n=2). **(I)** Western blot for B7H3 knockdown in NCI-PC155 organoids. **(J)** Dose response curves for NCI-PC155 organoids after B7H3 knockdown (sgB7H3 group). Error bars indicate the SEM.

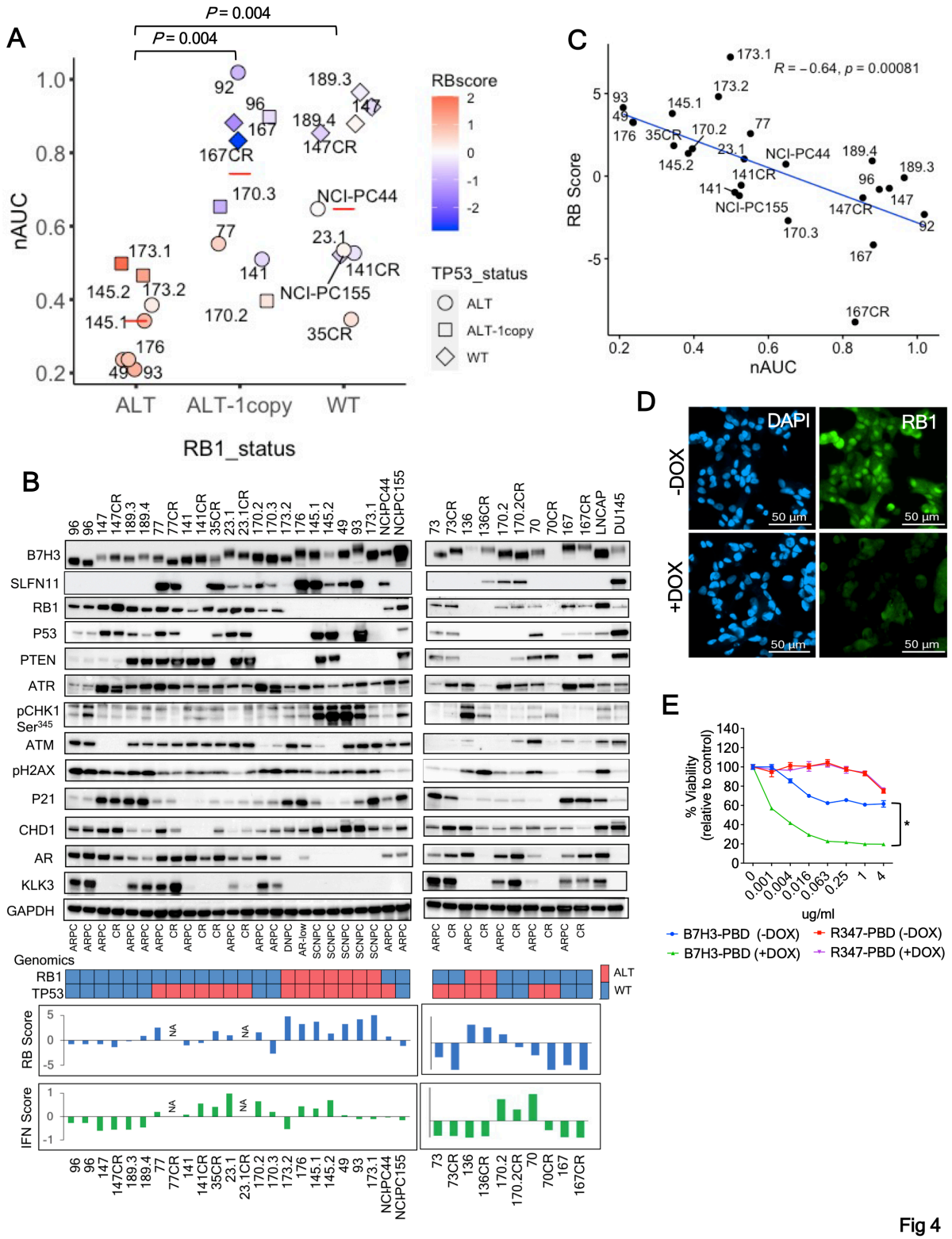

FIG. 4. RB1 loss predicts B7H3-PBD-ADC response. (A) B7H3-PBD-ADC response

categorized by *RB1* genomic status. Red line indicates the median nAUC for each group. *TP53* genotypes are shown as different shapes. Color indicates RB1 signature score on z-transformed scale. **(B)** Immunoblot analysis of organoid models and prostate cancer cell lines for the indicated markers. Heatmap (bottom) showing *RB1* and *TP53* genomic status. For *RB1*, red color indicates biallelic copy loss and blue indicates wild-type or 1 copy loss. *TP53* status in red refers to alterations by bi-allelic inactivation or gain of function mutation and in blue indicates wild-type or monoallelic loss. Bar plots for RB1 and IFN signature scores are shown for the organoid models. **(C)** Correlation of B7H3-PBD-ADC response (nAUC) and RB1 signature score. Pearson's correlation coefficient r = -0.64, $P = 0.00081$. **(D)** IF images confirming DOX-inducible knockdown of RB1 in LuCaP167 organoid model. **(E)** B7H3-PBD-ADC dose response curves in LuCaP167 ($RB1^+$) organoid model expressing DOX inducible *RB1* shRNA. Error bars indicate the SEM. $^*P < 0.05$.

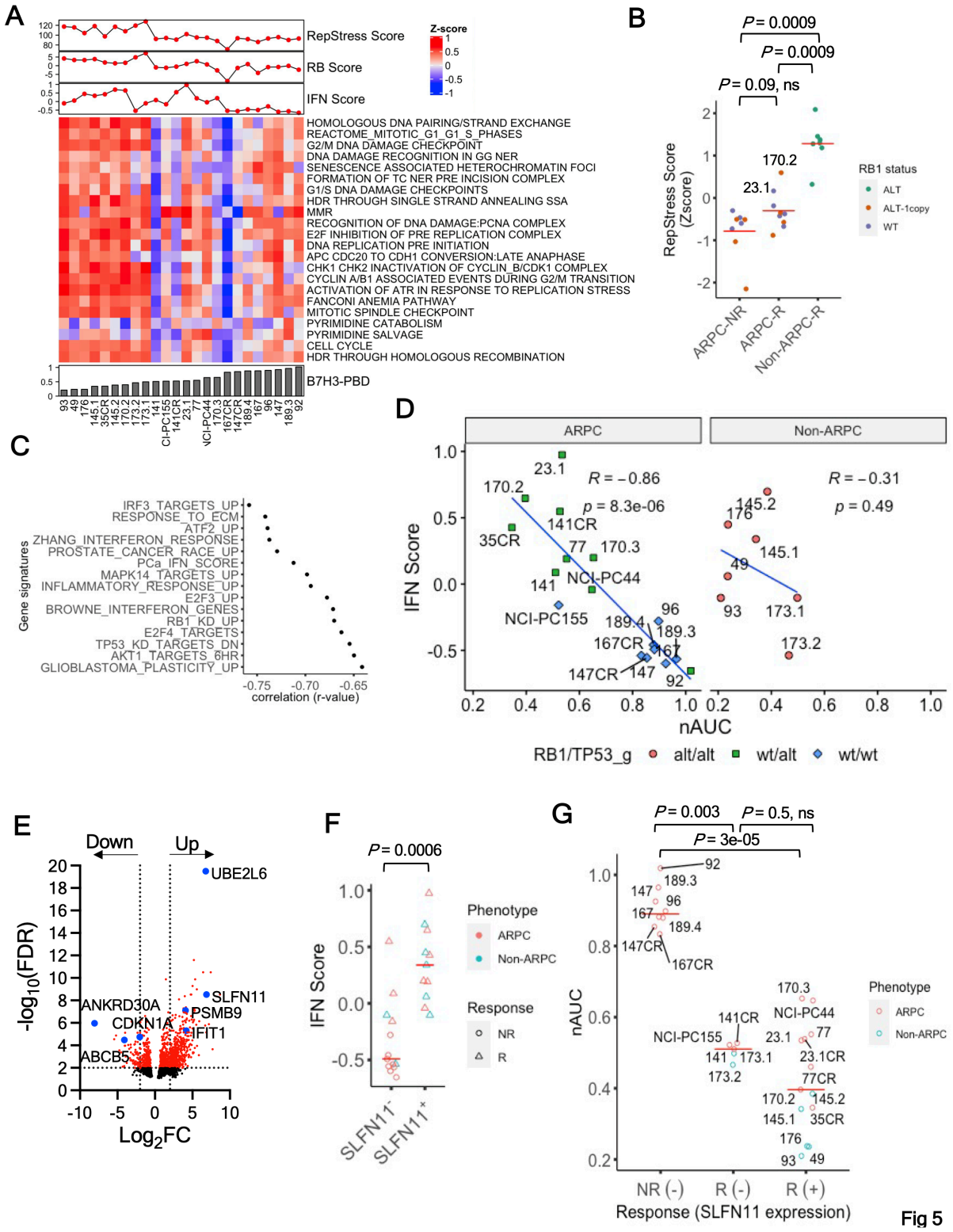
A
RepStress Score
RB Score
IFN Score
Z-score
HOMOLOGOUS DNA PAIRING/STRAND EXCHANGE
REACTOME_MITOTIC_G1_G1_S_PHASES
G2/M DNA DAMAGE CHECKPOINT
DNA DAMAGE RECOGNITION IN GG NER
SENESCENCE ASSOCIATED HETEROCHROMATIN FOCI
FORMATION OF TC NER PRE INCISION COMPLEX
G1/S DNA DAMAGE CHECKPOINTS
HDR THROUGH SINGLE STRAND ANNEALING SSA
MMR
RECOGNITION OF DNA DAMAGE:PCNA COMPLEX
E2F INHIBITION OF PRE REPLICATION COMPLEX
DNA REPLICATION PRE INITIATION
APC CDC20 TO CDH1 CONVERSION:LATE ANAPHASE
CHK1 CHK2 INACTIVATION OF CYCLIN_B/CDK1 COMPLEX
CYCLIN A/B1 ASSOCIATED EVENTS DURING G2/M TRANSITION
ACTIVATION OF ATR IN RESPONSE TO REPLICATION STRESS
FANCONI ANEMIA PATHWAY
MITOTIC SPINDLE CHECKPOINT
PYRIMIDINE CATABOLISM
PYRIMIDINE SALVAGE
CELL CYCLE
HDR THROUGH HOMOLOGOUS RECOMBINATION
B7H3-PBD
B
P= 0.0009
P= 0.0009
P= 0.09, ns
RepStress Score (Zscore)
RB1 status
ALT
ALT-1copy
WT
ARPC-NR
ARPC-R
Non-ARPC-R
C
Gene signatures
IRF3_TARGETS_UP
RESPONSE_TO_ECM
ATF2_UP
ZHANG_INTERFERON_RESPONSE
PROSTATE_CANCER_RACE_UP
PCa_IFN_SCORE
MAPK14_TARGETS_UP
INFLAMMATORY_RESPONSE_UP
E2F3_UP
BROWNE_INTERFERON_GENES
RB1_KD_UP
E2F4_TARGETS
TP53_KD_TARGETS_DN
AKT1_TARGETS_6HR
GLIOBLASTOMA_PLASTICITY_UP
correlation (r-value)
D
ARPC
Non-ARPC
R = −0.86
p = 8.3e-06
R = −0.31
p = 0.49
IFN Score
nAUC
RB1/TP53_g
alt/alt
wt/alt
wt/wt
E
Down
Up
UBE2L6
SLFN11
PSMB9
IFIT1
ANKRD30A
CDKN1A
ABCB5
-log10(FDR)
Log2FC
F
P= 0.0006
IFN Score
Phenotype
ARPC
Non-ARPC
Response
NR
R
SLFN11-
SLFN11+
G
P= 0.003
P= 0.5, ns
P= 3e-05
nAUC
Phenotype
ARPC
Non-ARPC
NR (-)
R (-)
R (+)
Response (SLFN11 expression)

Fig 5

FIG. 5. Markers of B7H3-PBD-ADC sensitivity. (A) Heatmap of the pathways contributing to the replication stress (RepStress) signature score. Organoid models are ranked from left to right based on increasing B7H3-PBD nAUC (bottom panel). Top panel showing RepStress, RB-, and interferon (IFN) signature scores. **(B)** Comparison of z-transformed RepStress score in AD non-responders (ARPC-NR), ARPC responders (ARPC-R), and non-ARPC responders (NonARPC-R). Color indicates *RB1* genotype. **(C)** Univariate correlation analyses between nAUC and MsigDB gene signatures, including refined IFN signature score for prostate cancer labeled as "PCa_IFN_Score". Spearman correlation coefficient is shown for top significant gene sets. FDR ≤ 0.05. **(D)** Plot of IFN score and B7H3-PBD-ADC sensitivity (nAUC) for ARPC and non-ARPC models. Association with *RB1* and *TP53* status is shown by points of different shape and color. **(E)** Volcano plot for differentially expressed genes between B7H3-PBD-ADC responsive ARPC models vs non-responsive ARPC models. Dotted lines are shown for $\log_2$ fold change of -2 and 2 at FDR ≤ 0.01. **(F)** Comparison of IFN score with SLFN11 expression. **(G)** B7H3-PBD-ADC response categorized by SLFN11 expression. Red line indicates median nAUC for each group. NR = non-responder, R = responder, +/- indicates SLFN11 expression.

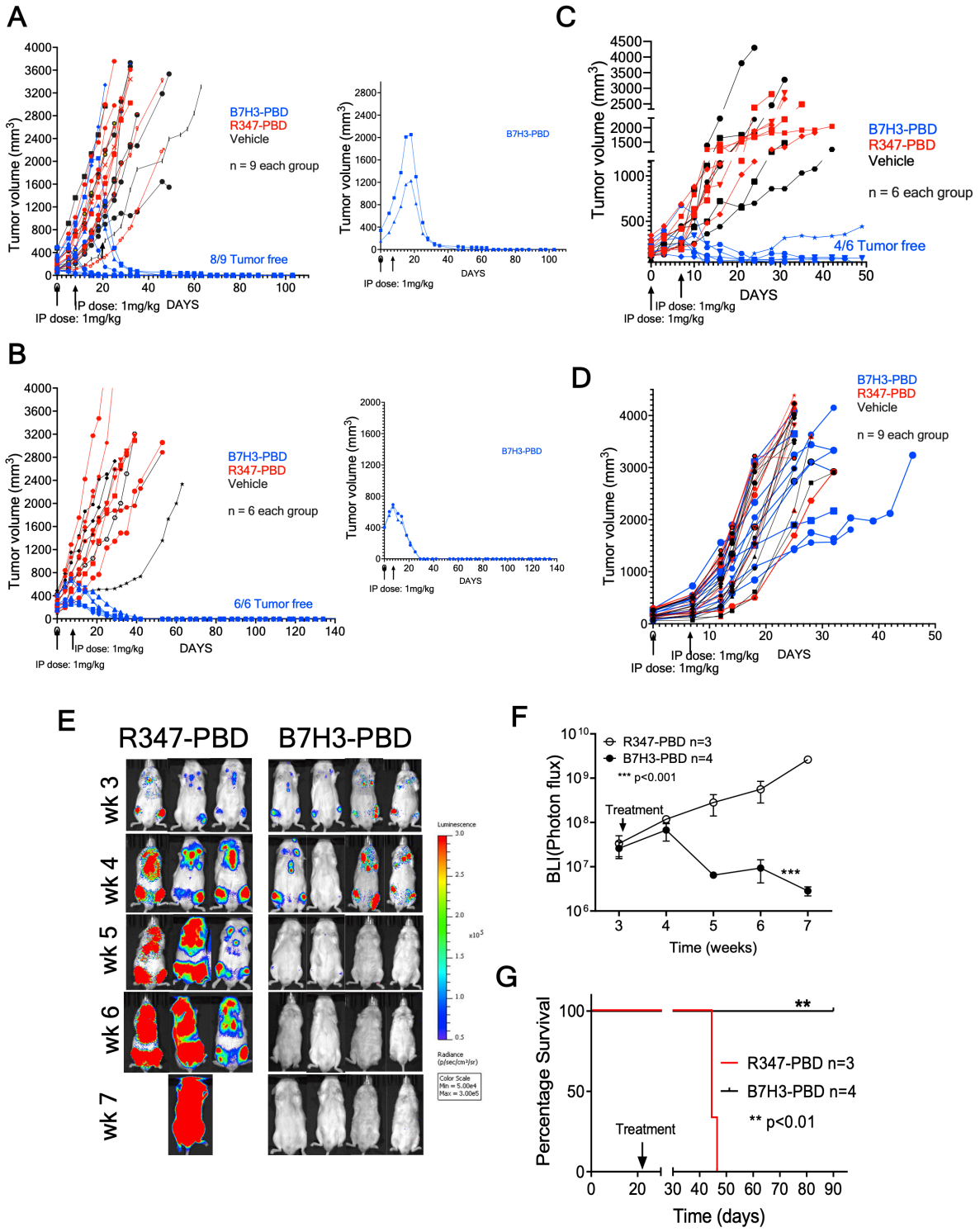

FIG. 6. Prostate cancer organoid-derived biomarkers associated with in vivo tumor

responses in preclinical trials of the B7H3-PBD-ADC. (**A-D)** Tumor response to B7H3-PBD-ADC (1mg/kg), R347-PBD-ADC (1mg/kg) or vehicle in the four selected LuCaP models based on identified biomarkers **(A)** LuCaP 145.2 (SCNPC phenotype; $RB1^{loss}$, $SLFN11^{+}$, IFN $score^{HIGH}$), n=9 / group. **(B)** LuCaP 136 (ARPC phenotype; $RB1^{loss}$, $SLFN11^{-}$, IFN $score^{low}$), n = 6/ group. **(C)** LuCaP 77 (ARPC, $RB1^{+}$, $SLFN11^{+}$, IFN $score^{medium}$) n = 6 /group. **(D)** LuCaP 167 (ARPC, $RB1^{+}$, $SLFN11^{-}$, IFN $score^{low}$) n = 9 /group. Right panels for (A) and (B) displaying antitumor activity of B7H3-PBD-ADC in mice with large established tumors (145.2; >1000 mm^3 and 136; >650 mm^3). Tumor volume measurements (mm^3) are shown from the time of first treatment. Arrows indicate once weekly dose for 2 weeks. **(E)** Bioluminescence imaging of LuCaP 136 metastases following treatment with B7H3-PBD-ADC (n = 4) or R347-PBD-ADC (n=3). Mice were treated once weekly for two weeks. **(F)** Average BLI for treated mice from the time of first treatment. Means ± standard deviation, Two-way ANOVA test; $P < 0.001$. (G) Kaplan-Meier survival analysis for the B7H3-PBD-ADC and R347-PBD-ADC treated LuCaP 136 metastases. Log-rank test ($P < 0.01$).

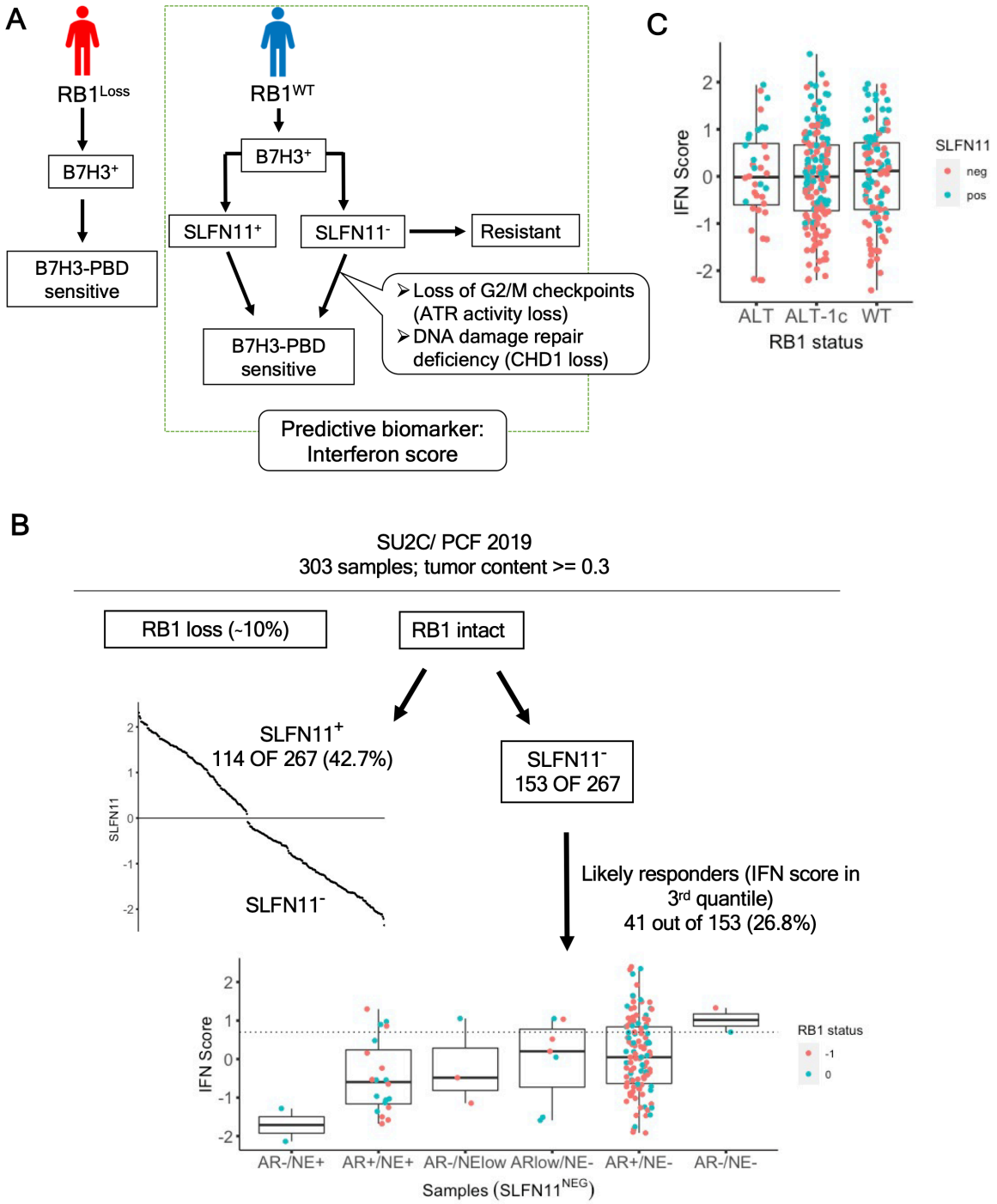

Fig 7

FIG. 7. (A) Schematic of proposed biomarker based therapeutic decisions for B7H3-PBD-ADC

treatment of CRPC patients. **(B)** Relationship between z-transformed IFN score, *RB1* status, and *SLFN11* expression in SU2C/PCF 2019 dataset. Log_2(FPKM1+1) mean centered values are plotted for *SLFN11* expression after ordered quantile normalization. Box plots are showing IFN score on z-transformed scale for *SLFN11* negative samples. Dotted line on the bar plot indicates 3rd quantile. Patient samples are categorized based upon ARPC and SCNPC phenotypes defined by Nyquist et al (9). **(C)** Analysis of SU2C data to predict likely responders based on *RB1* and *SLFN11* status, and IFN score.

Table 1. B7H3-PBD response data, and molecular features of 26 mCRPC models.

	PDXO	nAUC	IC50 ng/ml	RB score	RepStress score	IFN score	RB1 protein	RB1 genomic status	TP53 Protein	TP53 Genomic status	SLFN11 Protein	B7H3 protien (x10)	AR score	phenotype
	Non-ARPC													
1	93	0.21	0.36	4.15	117.42	-0.10	DEF	ALT	EXP_GAIN	ALT_GOF	+	9.74	-0.13	NE
2	49	0.24	0.03	3.27	115.83	0.06	DEF	ALT	DEF	ALT	+	9.25	-0.16	NE
3	176	0.24	0.13	3.24	104.23	0.45	DEF	ALT	DEF	ALT	+	10.46	-0.07	AR-low
4	145.1	0.34	1.21	3.79	118.34	0.34	DEF	ALT	EXP_GAIN	ALT_GOF	+	2.72	0.03	NE
6	145.2	0.39	1.20	1.37	117.11	0.70	DEF	ALT	EXP_GAIN	ALT_GOF	+	2.56	-0.28	NE
9	173.2	0.47	2.08	4.81	119.40	-0.54	DEF	ALT	DEF	ALT-1copy	-	2.53	-0.30	DNPC
10	173.1	0.50	0.22	7.21	127.93	-0.10	DEF	ALT	DEF	ALT-1copy	-	5.61	-0.29	NE
	ARPC-R													
5	35CR	0.35	0.48	1.84	97.52	0.43	EXP	WT	EXP_GAIN	ALT_GOF	+	24.10	0.70	AD-CR
7	170.2	0.40	1.45	1.66	107.98	0.65	EXP	ALT-1copy	DEF	ALT-1copy	+	21.18	0.67	AD
8	77CR	0.46	1.46	NA	NA	NA	EXP	ALT-1copy	EXP_GAIN	ALT_GOF	+	7.07	NA	AD-CR
11	141	0.51	5.25	-0.98	92.31	0.09	EXP	ALT-1copy	DEF	ALT	-	19.64	0.63	AD
12	NCI-PC155	0.52	8.71	-1.18	94.28	-0.16	EXP	WT	EXP	WT	-	19.99	0.78	AD
13	141CR	0.53	5.67	-0.55	90.91	0.55	EXP	WT	DEF	ALT	-	7.13	0.52	AD-CR
14	23.1	0.54	2.91	1.04	102.17	0.97	EXP	WT	EXP_GAIN	ALT	+	3.02	0.62	AD
15	23.1CR	0.54	8.31	NA	NA	NA	EXP	WT	EXP_GAIN	ALT	+	1.19	NA	AD-CR
16	77	0.55	3.15	2.58	95.31	0.19	EXP	ALT-1copy	EXP_GAIN	ALT_GOF	+	5.63	0.75	AD
17	NCI-PC44	0.65	9.11	0.72	94.96	-0.04	EXP	WT	DEF	ALT	+	1.27	0.85	AD
18	170.3	0.65	11.17	-2.70	88.20	0.20	EXP	ALT-1copy	DEF	ALT-1copy	+	10.15	0.73	AD
	ARPC-NR													
19	167CR	0.83	UND	-8.83	71.25	-0.54	EXP	ALT-1copy	EXP	WT	-	7.66	0.54	AD-CR
20	147CR	0.85	UND	-1.31	93.73	-0.56	EXP	WT	EXP	WT	-	4.11	0.78	AD-CR
21	189.4	0.88	UND	0.93	91.95	-0.46	EXP	WT	EXP	WT	-	5.32	0.72	AD
22	167	0.88	UND	-4.16	86.14	-0.49	EXP	ALT-1copy	EXP	WT	-	4.65	0.44	AD
23	96	0.90	UND	-0.80	93.23	-0.28	EXP	ALT-1copy	EXP	ALT-1copy	-	6.05	0.78	AD
24	147	0.93	UND	-0.74	95.97	-0.60	EXP	WT	EXP	WT	-	3.33	0.69	AD
25	189.3	0.97	UND	-0.09	90.22	-0.56	EXP	WT	EXP	WT	-	6.70	0.49	AD
26	92	1.02	UND	-2.32	93.10	-0.65	**NA**	ALT-1copy	**NA**	ALT	-	11.46	0.73	AD

B7H3-PBD-ADC (nAUC and IC50), **UND** = undertermined, **NA** = data not available, **ARPC-R** = Adenocarcinoma responders, **ARPC-NR** = Adenocarcinoma non-responders, **EXP** = expressed, **DEF** = deficient, **EXP_GAIN** = Protein expression due to gain of function (GOF) mutation